Article

Graphene Oxide Decorated with Ag and CeO$_2$ Nanoparticles as a Catalyst for Room-Temperature 4-Nitrophenol Reduction

Aleksey Taratayko [1], Ekaterina Kolobova [2] and Grigory Mamontov [1,*]

[1] Research Laboratory of Porous Materials and Sorption, Department of Chemistry, Tomsk State University, Tomsk 634050, Russia

[2] Laboratory "Chemical Engineering and Molecular Design", Research School of Chemical and Biomedical Technologies, Tomsk Polytechnic University, Tomsk 634034, Russia

[*] Correspondence: grigoriymamontov@mail.ru; Tel.: +7-913-883-5124

Abstract: Catalytic reduction of nitroaromatic compounds (NCs) into corresponding aminoaromatic compounds (ACs) addresses two challenges: enhancing of the manufacture scale of ACs as valuable chemical intermediates and removal of NCs as widespread wastewater pollutants. Among the noble metal catalysts that feature low-temperature activity, chemical stability, and nontoxicity, silver-containing catalysts are attractive as cost-efficient and easily prepared compositions. This paper is devoted to the design and study of efficient and environmentally benign Ag- and CeO$_2$-containing NCs reduction catalysts supported on graphene oxide (GO). The silver- and/or ceria-containing catalysts are synthesized using deposition-precipitation onto GO prepared by oxidative treatment of graphite. The catalysts and support are characterized by XRD, XPS, TGA, N$_2$ sorption, Raman spectroscopy, and UV–VIS spectrometry. The influence of state and the interaction of the active components on catalytic activity is thoroughly estimated in 4-nitrophenol (4-NP) reduction into 4-aminophenol (4-AP) at ambient pressure and room temperature. Nanosized Ag and CeO$_2$ particles with sizes up to 30 and 5 nm, respectively, in the GO structure are obtained. The co-deposition of Ag and CeO$_2$ onto GO promotes the stabilization of silver in the catalyst. The Ag-CeO$_2$/GO catalyst demonstrates superior activity in the synthesized series (k_{app} of 1.615 and 3.674 min^{-1} for as-prepared and pre-reduced samples). In addition, the Ag-CeO$_2$/GO catalyst retains good stability and a low leaching degree of the active components that makes these compositions efficient in NCs' reduction into corresponding ACs.

Keywords: graphene oxide; Ag nanoparticles; 4-nitrophenol reduction; mild conditions; CeO$_2$

1. Introduction

Nowadays, nitroaromatic compounds (NCs or nitroarenes) are among the largest and most important groups of industrial chemicals used, whose production capacity is 9% of all benzene derivatives. The NCs are feedstocks for a set of materials: explosives, pesticides, biologically active substances, etc. However, the vast NC amount (>75%) is used in the manufacturing of aminoaromatic compounds (ACs or aminoarenes) [1,2]. A classical and the most widespread method of AC production is NC catalytic reduction, realized by such chemical companies as BASF, Bayer (gas-phase process), and DuPont (liquid-phase process). Copper-containing catalysts, e.g., Cu/SiO$_2$ and Cu/Cr$_2$O$_3$, are favored for the gas-phase process, while noble metal (platinum and palladium)-containing catalysts are preferred for the liquid-phase process [3–5]. In turn, ACs are valuable intermediates in the manufacturing of pharmaceuticals, dyes and pigments, plastics (polyurethanes), and agrichemicals, which are also used as curing agents and antioxidants in synthetic rubbers [6]. Thus, NCs' conversion into corresponding ACs is an important up-to-date chemical process affecting a number of human life aspects.

However, NCs are considered among the most widespread toxic and carcinogenic organic pollutants due to their versatile applications. They can be accumulated in the atmosphere, soil, and water. NCs occur in the environment substantially due to anthropogenic sources (agriculture, industrial wastewaters, storage leaks, fossil fuels combustion, etc.) and less due to natural sources (solar-induced nitration of water-dissolved arenes, vital activity of some microorganisms) [1]. There are a number of ecologically safe methods resolving NC pollution, namely chemical treatment by oxidizers (e.g., ozone [7]), electro- and photocatalytic degradation [8], and bioremediation [2] of dissolved nitroarenes. However, these approaches are destructive, i.e., they cause total decomposition and loss of the compounds, and can be economically costly. At the moment, the NCs' catalytic reduction to aminoarenes is considered a promising method [9]. This approach allows following the extraction of the substances from a solution using adsorbents or chemical bonding. The obtained aromatic amines can be further recycled into useful feedstocks, which is a more profitable process of removing the NCs from the environment. Therefore, both the growing AC demand and NC removal are urgent challenges in the field of the design of novel catalysts for selective NC reduction.

Particular success in solving these challenges was achieved using noble metal catalysts, i.e., Au, Pt, Pd, and Ag, that demonstrate high catalytic activity under mild conditions, stability, and nontoxicity [10,11]. Silver-containing catalysts are currently used in a number of industrial catalytic processes, such as alcohol oxidation to aldehydes [12], ethylene glycol oxidation to glyoxal, and ethylene epoxidation, with the last one being a process in which Ag-containing catalysts do not have analogues [13]. Unlike platinum-group metals, metallic silver has lower sorption and affinity to hydrogen due to the totally occupied 4d electron shell. This limits silver use in large-scale reduction processes. Nevertheless, Ag-based catalysts are a recent focus of catalytic science [14]. Among the noble metals used in reduction reactions, these are advantageous catalytic systems due to the relatively low cost, facile preparation procedure, and wide opportunities for modification [15]. To the best of our knowledge, the work of Pradhan et al. [16] was one of the earliest thorough research projects devoted to NC reduction with $NaBH_4$ using silver nanoparticles as a catalyst. The reaction is representative of screening the catalytic properties of catalysts used in hydrogenation processes due to a simple instrumental design and methodology and mild reaction conditions [9].

The design of metal-containing catalysts supported on transition metal oxides is a widespread technique for achieving desirable catalytic properties. Cerium (IV) oxide, a transition metal oxide with a cubic fluorite-like lattice, is an attractive compound to prepare supported metal catalysts, which is characterized by the presence of the dynamic Ce^{4+}/Ce^{3+} redox pair [17]. This fact results in cerium (IV) oxide's own catalytic activity and surface defects continuum acting as an active site to stabilize metal species in the dispersed state [18]. Ag-CeO_2 is a promising composition since the metal–support interaction (MSI) between silver and ceria leads to the cooperative action of the metal and the oxide active sites in catalytic reactions and also to modifying of the state of the components at the Ag-CeO_2 interface [19,20]. This causes a synergistic effect in both oxidation [21–23] and reduction [24–26] reactions, enhancing catalytic activity. However, the Ag-CeO_2 system tends to aggregate during the synthesis and catalysis procedure, and there is a demand for primary support to prevent the active surface from decreasing.

In the past few years, carbonaceous and carbon-based nanomaterials have been attracting profound research interest. Graphene is a 2D carbon nanomaterial consisting of a single layer of sp^2-hybridized carbon formed in a hexagonal lattice. Although the term "graphene" was introduced in 1986, only in 2004 did Andre Geim and Konstantin Novoselov successfully obtain and study the isolated graphene layer [27]. There has been a dramatic growth in the number of publications devoted to graphene-based materials since 2010, when the authors were awarded the Nobel Prize in Physics. The material has unique physical-chemical properties, such as a high specific surface area (up to 2000 m^2/g), thermal conductivity (~5000 W/m·s), intrinsic mobility (~200,000 cm^2/V·s), mechanical

strength (Young modulus ~1 TPa), chemical stability, and biocompatibility [28]. Graphene-based materials are in focus in numerous scientific areas: from electronics and energy storage/conversion to medicine and environmental applications [29,30]. Graphene derivatives, graphene oxide (GO) and reduced graphene oxide (rGO), are of interest in the field of catalysis science, where they are used as supports for active components [28,31] and adsorbents [32,33]. GO is a nonstoichiometric carbon-based material synthesized by oxidative treatment of graphite, followed by exfoliation, and contains abundant oxygen functional groups: carboxyl, carbonyl, hydroxyl, and epoxy groups. When the obtained material is reduced, an rGO material is obtained with a structure similar to pristine graphene but with certain matrix defects (vacancy, nanopore, Stone–Wales defect) and a few residual oxygenated moieties [34]. The use of GO and rGO as supports for catalysts and adsorbents is due to a number of properties. Apart from a high surface area and chemical stability, the occupation of the GO surface by functional groups makes it hydrophilic, which simplifies its use in an aqueous medium, increases its sorption capacity toward polar substances (including precursors), and also provides opportunities for surface functionalization [30,34]. Moreover, optical activity and semiconductive properties are characterized by a decrease in the band gap value from ~4.3 to ~1.1 eV upon GO-to-rGO reduction, which allows use of these materials as active supports in electro- and photocatalysts [35,36].

Among a variety of graphene-based composites, the $Ag-CeO_2$ catalysts supported on GO or rGO have been studied in the reduction of nitroaromatic compounds [37], the photocatalytic esterification of aldehydes [38], the degradation of organic pollutants [39,40], etc. The authors used consequent loading of the active components onto GO or the use of additional stabilizing agents (PVP, 6-aminohexanoic acid) to synthesize supported $Ag-CeO_2$ catalysts. Unlike the methods described in these papers, the Ag^+ and Ce^{3+} precursors are co-deposited onto GO for an efficient $Ag-CeO_2$ junction via the redox reaction between the precursors during the synthesis [22,24]. In addition, the synthesis was carried out in the absence of additional stabilizers to avoid impurities and gain a chemically defined composition of the catalysts.

Thus, this work focuses on designing and studying efficient and environmentally benign $Ag-CeO_2$/GO catalysts for NC reduction. Special attention is given to the effect of Ag and CeO_2 co-deposition onto GO. The influence of state and the interaction of active components on catalytic activity is estimated during 4-nitrophenol's (4-NP) reduction into 4-aminophenol (4-AP) at ambient pressure and room temperature.

2. Results and Discussion

2.1. Characterization of the Support

2.1.1. N_2 Sorption

The textural characteristics of the porous structure of the synthesized support were studied by the method of low-temperature adsorption-desorption of nitrogen. Figure S1 shows the results for milled GO and pristine graphite. The GO sorption isotherm (Figure S1a) refers to type IV isotherms with a H3 hysteresis loop according to the IUPAC classification [41]. This type of isotherm is characterized by a hysteresis loop in the relative pressure range of 0.45–0.99 and a sharp rise in the initial section of the adsorption branch in the range of low pressures (P/P_o < 0.05), which indicate a micro-mesoporous layered structure of the obtained material. Unlike the synthesized GO, graphite is a non-porous material. A low value of nitrogen sorption is observed up to a relative pressure of 0.85, above which polymolecular adsorption begins on the surface of the graphite particles. The pore size distribution shows that GO has a narrow distribution of micropores (0.35–0.6 nm in size), with a small contribution of pores with a size of 0.6–0.8 nm (Figure S1b), while mesopores have a continuous descending distribution with the majority of pores being in the range of 1.75–3.5 nm. The bimodal pore size distribution is due to the formation of microporous aggregates of folded turbostratic carbon layers ("stacks") that are separated by mesopores [41].

Table 1 summarizes the textural characteristics of GO and graphite samples. The synthesized support possesses a surface area of 54.6 m^2/g and a pore volume of 0.1 cm^3/g, which is much higher than that of the initial graphite. The volume of micropores for GO is 0.02 cm^3/g (~20% of the total pore volume). The micropores with an average size of 0.45 nm have a specific surface area of 46 m^2/g (~85% of the total surface). Hence, the main contribution to the surface area of the obtained support is caused by micropores.

Table 1. Textural characteristics of the carbon materials.

Sample	S_{BET} (m^2/g)	V_{pore} (cm^3/g)	Pore Width (nm)	S_{micro}* (m^2/g)	V_{micro}* (cm^3/g)	D_{micro}* (nm)
GO	54.6	0.10	5.23	46	0.02	0.45
Graphite	0.46	0.02	-	-	-	-

* Calculated by the Horvath-Kawazoe method.

2.1.2. XRD

The phase composition of the graphene derivatives was studied by powder X-ray diffraction. Figure 1 shows the XRD patterns of graphite, GO, and rGO. A graphite sample is characterized by reflections, with maxima at 26.5°, 42.5°, 44.6°, and 54.5° 2θ that are attributed to the crystallographic planes of the graphite hexagonal lattice (PDF 00-041-1487): d_{002} = 3.37 Å, d_{100} = 2.13 Å, d_{101} = 2.03 Å, and d_{004} = 1.68 Å, respectively. The extremely high intensity and small width of the peaks indicate the large size of the crystallites, which in turn leads to a low surface area and porosity observed from the nitrogen sorption results.

For the synthesized GO sample, a shift of the (002) reflection attributed to the interlayer space of the sp^2-hybridized carbon is observed at 11.1° 2θ that corresponds to the interplanar distance d_{002} = 7.98 Å. The increase in the distance between the carbon sheets is due to the intercalation of the oxygenated moieties and adsorbed water into the interlayer space as a result of the oxidative treatment of graphite [42]. The broadening of the interlayer space causes the appearance of microporosity in the sample, which is consistent with the nitrogen sorption data. The high intensity and pointed shape of the (002) reflection at 11.1° 2θ indicate the formation of ordered GO "stacks" with a uniform distribution of the embedded functional groups. The small peak at ~26° 2θ is attributed to the impurity phase of residual graphite.
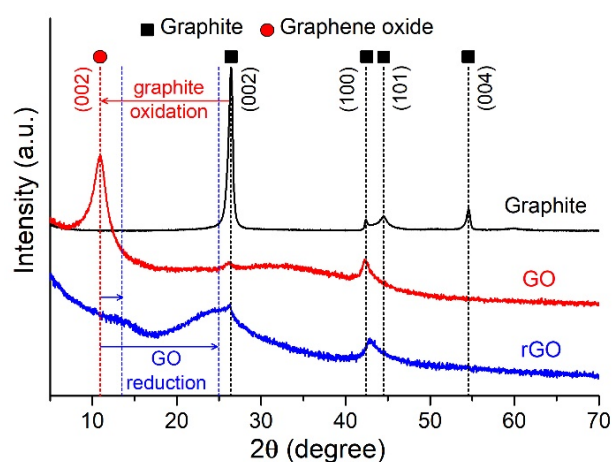

Figure 1. XRD patterns of graphite, GO, and rGO samples.

When GO is reduced to rGO, the interlayer spacing decreases due to the elimination of functional groups, and the (002) reflection shifts to the region of large 2θ values: ~13° (partially reduced GO layers) and ~25° 2θ (reduced GO layers) [42]. These two peaks are observed since rGO does not have a specific distribution of the stable residual oxygenated moieties that cannot be removed without damaging the basal plane [34]. The higher intensity of the peak at ~25° 2θ may indicate a low content of oxygen functional groups in

the sample. A wide shape (halo) of the peak in the range of 18°–33° 2θ is associated with the inhomogeneous arrangement of the rGO layers. The absence of graphite reflections at (101) and (004) for GO and rGO is associated with the longitudinal displacement of the carbon layers relative to each other (turbostratic structure). The peak (100) is preserved and almost does not change its position in all samples, since it is formed by diffraction on parallel rows of carbon atoms within one layer.

Therefore, XRD allows identifying graphene derivatives, and the (002) reflection (its position and width) is characteristic for its various forms. Based on the observed decrease in the intensity and broadening of the (002) reflection, the structure order decreases in the graphite–GO–rGO series, which, in turn, is due to the distortion of the mutual arrangement of the carbon layers.

2.1.3. TGA

The thermal properties of graphene derivatives in oxidizing (air) and inert (argon) media were studied by thermogravimetric analysis. Figure 2 shows thermogravimetric curves (a) and corresponding DSC profiles (b). Pristine graphite exhibits the highest thermal stability, and weight loss occurs only in an oxidizing medium at temperatures above 700 °C (combustion process).
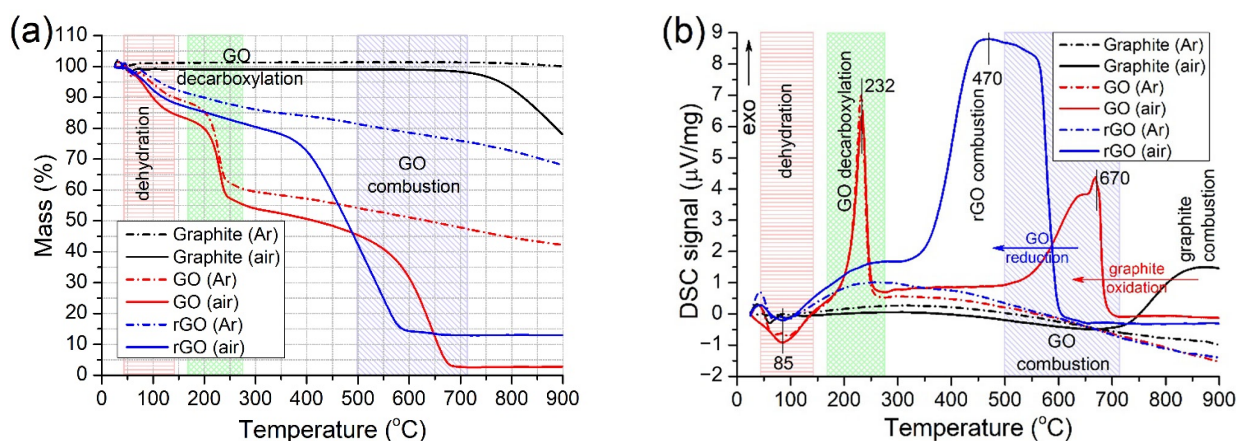

Figure 2. TG curves (**a**) and DSC profiles (**b**) of graphite, GO, and rGO samples in air and argon atmospheres.

The synthesized GO sample is characterized by three stages of weight loss in an air atmosphere. A 10–15 wt.% weight loss below 145 °C with an inflection point at 85 °C is attributed to endothermic dehydration. A further intensive weight loss of ~28 wt.% indicates an exothermic decarboxylation process (removal of labile carboxyl and carbonyl groups) between 165 and 275 °C, with an inflection point at 232 °C [43]. Decarboxylation is a characteristic process for graphene oxide and is retained when the sample is heated in both oxidizing and inert media [44]. The final gradual weight loss stage is an exothermic combustion observed in the range from 500 to 710 °C.

When GO is reduced to rGO, the stage of weight loss associated with the decarboxylation disappears due to the reduction of carboxyl and carbonyl groups. Moreover, the weight loss attributed to dehydration decreases to 7–11 wt.%. These facts denote a more hydrophobic character of rGO due to a much lower number of polar functional groups. The rGO combustion temperature region shifts toward a lower temperature range of 350–600 °C. It is noteworthy that a gradual weak mass decrease above 300 °C accompanied by an endothermic effect is observed in an argon atmosphere for GO and rGO, which may be associated with the removal of stable oxygenated moieties [43].

Thus, TGA, as XRD, is a method of identifying various graphene derivatives by the presence/absence of certain steps of weight loss and their temperature regions. Knowing the thermal properties of certain forms of graphene is also necessary to understand their applicability in various processes in order to avoid material destruction and loss of required properties. A greater shift in the combustion temperature toward lower values occurs

in the graphite–GO–rGO series. The revealed pattern is consistent with the XRD results: a decrease in the ordering and a more defective structure of carbon layers favor a more developed contact with the oxidizing medium and a lower temperature of oxidation.

2.2. Characterization of Catalysts

2.2.1. XRD

The phase composition of the silver- and/or ceria-containing catalysts prepared based on GO was studied by powder X-ray diffraction. Figure 3 shows the XRD patterns of the samples in the range of diffraction angles 2θ from 5° to 70°. For Ag/GO and Ag-CeO$_2$/GO catalysts, the reflections with maxima at 38.1°, 44.3°, and 64.4° 2θ correspond to the face-centered cubic (fcc) lattice of the metallic silver phase (PDF 01-071-6549): d_{111} = 2.36 Å, d_{200} = 2.04 Å, and d_{220} = 1.44 Å, respectively. In addition, the CeO$_2$/GO and Ag-CeO$_2$/GO samples feature reflections at 28.5°, 33.0°, 47.3°, and 56.2° 2θ, corresponding to a fluorite-type cubic lattice of the cerium (IV) oxide phase (PDF 01-079-6885): d_{111} = 3.12 Å, d_{200} = 2.71 Å, d_{220} = 1.92 Å, and d_{311} = 1.63 Å, respectively. The impurity phase of graphite in the catalysts is characterized by the presence of a reflection at 26.4° 2θ. Thus, as a result of the preparation of catalysts, the required phase composition of the active components is achieved.
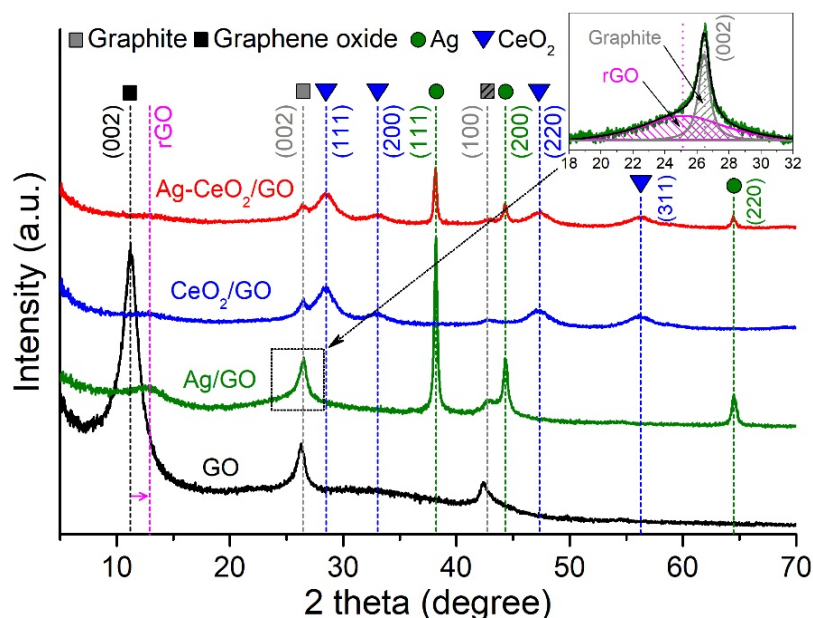

Figure 3. XRD patterns of the synthesized catalysts.

When Ag and CeO$_2$ are deposited on GO, the characteristic reflection (002) of the latter at ~11° 2θ disappears turning into a weakly intense peak at ~13° 2θ. Deconvolution of the peak at 26.4° 2θ for the Ag/GO catalyst (insertion in Figure 4) also shows the presence of a second low-intensity peak with a maximum at ~25° 2θ. The observed peaks are similar to those for the rGO sample (Figure 1) and belong to the GO layers of different reduction degrees, which, in turn, may indicate the process of GO partial reduction as a result of the synthesis of supported catalysts. Similar peaks are observed in [37] for silver- and/or ceria-containing catalysts. A substantial intensity decrease in these peaks with the active components' mass increasing is associated with the wedging action of Ag and CeO$_2$ nanoparticles on the carbon layers and their distortion, which leads to greater inhomogeneity of the interlayer space [45].
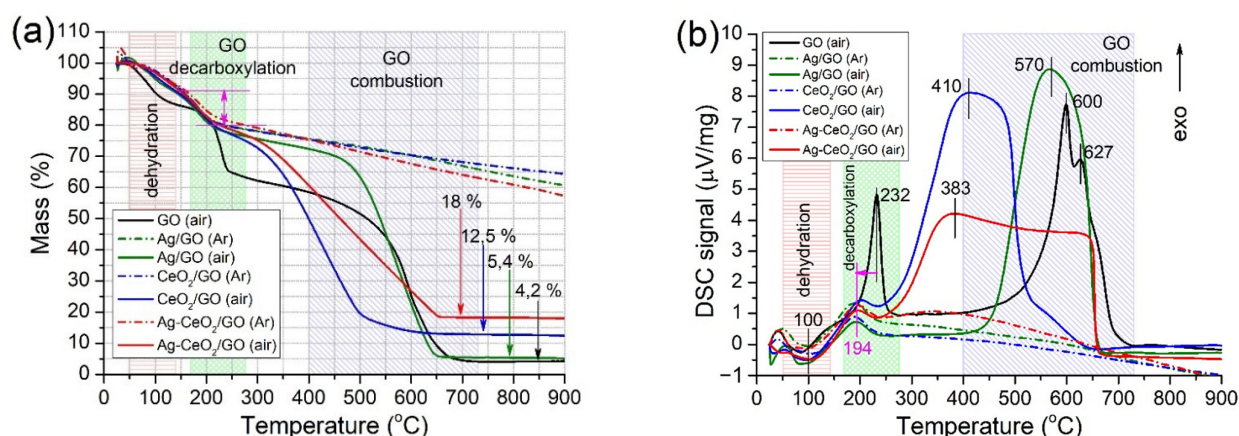
Figure 4. TG curves (**a**) and DSC profiles (**b**) of the GO-based catalysts in air and argon atmospheres.

Table 2 shows the data of particle size calculations for the synthesized support and catalyst samples. Based on the calculation of the (002) reflection for GO, it can be concluded that the carbon layers are organized in "stacks" with an average thickness of 5.0 nm, which is ~6–7 layers of graphene. In the catalysts, CeO_2 particles are stabilized in a highly dispersed state in the CeO_2/GO and Ag-CeO_2/GO samples: 5.0 and 5.3 nm, respectively. In contrast, according to XRD results, the silver particles have an average size of ~30 nm in the Ag-containing catalysts. The larger size of the Ag particles can be due to the weaker adsorption of the silver precursor (Ag^+) on the negatively charged deprotonated GO surface than the more charged Ce^{3+}, which leads to nonuniform deposition, low nucleation, and intense crystallite growth. However, the reduction of the silver precursor to the metallic state is possible in the presence of GO at the US treatment stage that also leads to the formation of large particles [46]. At the same time, it is noteworthy that the silver diffraction peaks are broadened at the base, which may indicate the presence of smaller silver particles in the samples. Thus, the presence of small Ag NPs with sizes of a few nanometers in the sample is possible.

Table 2. Results of XRD calculations for the synthesized samples.

Sample	Phase	Calculated Reflection (*hkl*)	Interplanar Distance *d* (Å)	Particle Size *D* (nm)
GO	GO (hex.)	(002)	7.98	5.0
Ag/GO	Ag (cub.)	(111)	2.36	27.5
CeO_2/GO	CeO_2 (cub.)	(111)	3.12	5.0
Ag-CeO_2/GO	Ag (cub.)	(111)	2.36	29.3
	CeO_2 (cub.)	(111)	3.12	5.3

2.2.2. XPS

The elemental composition of the synthesized catalysts and graphene derivatives was investigated by X-ray photoelectron spectroscopy with recording of the survey XPS spectra. The analysis data are summarized in Table 3. GO possesses abundant oxygenated moieties, and the C:O atomic ratio equals 2.75. Deconvolution of the C 1s region high-resolution XPS spectrum of GO (Figure S2a) demonstrates diverse carbon chemical states: basal carbon C=C (284.1 eV) and C–C (284.8 eV), epoxy C–O–C (286.6 eV), carbonyl C=O (288.1 eV), carboxyl O–C=O (288.9 eV) groups, and $\pi \rightarrow \pi^*$ satellite (290.9 eV) [47,48]. When the GO material undergoes reduction by $NaBH_4$, the C:O atomic ratio substantially decreases to 6.57 in the obtained rGO. A significant decrease in the total signal of the oxygenated carbon moieties from 61 to 23 at.% (the whole C 1s region signal is 100 at.%) and a corresponding increase in the total signal of the unoxidized carbon species from 36 to 75 at.% are observed in the rGO C 1s region (Figure S2b and Table S1). In addition, the peak maxima of epoxy and carboxyl groups in the rGO sample shift to 286.2 and 288.5 eV, respectively, which is attributed to the carbonyl and hydroxyl groups' contribution to the signals. These

facts indicate reduction of labile functional groups observed by XRD (Figure 1) and TGA (Figure 2) and the retaining of residual oxygenated moieties that cannot be removed without damaging the basal carbon plane. The synthesized catalysts are characterized by a number of C 1s peaks attributed to basal carbon C=C/C–C (284.6 eV), hydroxyl C–OH (285.5 eV), epoxy C–O–C (286.8 eV), carboxyl O–C=O (288.5 eV) groups, and $\pi \rightarrow \pi^*$ satellite (291.0 eV) (Figure S2c–e). The total signal of the oxygenated carbon moieties between 34 and 40 at.% (Table S1) certainly indicates an intermediate state of the support between GO and rGO observed by XRD (Figure 3). In addition, the distinguishable signal of hydroxyl groups in the catalysts may be due to the unzipping of epoxy groups and bonding of the formed hydroxyl groups to the deposited active components. In addition, the N 1s signal can be associated with adsorbed or chemically bonded nitrogen species as a result of $NH_{3\,(aq.)}$ use as a precipitant during catalyst synthesis.

Table 3. Elemental composition of the samples according to survey XPS spectra.

Sample	Calculated XPS Peaks				
	C 1s (at.%)	O 1s (at.%)	N 1s (at.%)	Ag 3d (at.%)	Ce 3d (at.%)
GO	73.36	26.64	-	-	-
rGO	86.79	13.21	-	-	-
Ag/GO	83.57	12.62	3.46	0.35	-
CeO$_2$/GO	77.44	17.74	4.14	-	0.67
Ag-CeO$_2$/GO	78.09	16.71	3.94	0.60	0.66

The Ce 3d percentage of 0.67 and 0.66 at.% corresponds to ~8.4 and ~8.0 wt.% of the deposited CeO$_2$ in the CeO$_2$/GO and Ag-CeO$_2$/GO catalysts, respectively. The obtained values mostly correlate with the calculated amount of ceria (10 wt.%) in the catalysts. With regard to the Ag 3d percentage, there is a significant difference in the values. The Ag 3d percentage of 0.35 and 0.60 at.% corresponds to ~2.9 and ~4.6 wt.% of the deposited Ag in the Ag/GO and Ag-CeO$_2$/GO catalysts, respectively. The Ag amount in the Ag-CeO$_2$/GO sample mostly correlates with the calculated one (5 wt.%) in contrast to that in the Ag/GO sample. These facts may be due to weaker adsorption of the Ag$^+$ precursor on the GO surface in comparison with Ce^{3+}. This results in a lower Ag amount in the Ag/GO sample and also a larger size of Ag particles than those of CeO$_2$ in the CeO$_2$/GO and Ag-CeO$_2$/GO samples observed by XRD. However, in the presence of CeO$_2$, the silver content in the Ag-CeO$_2$/GO sample is close to the theoretical one. Therefore, CeO$_2$ is a GO-modifying component, and the ceria surface acts as a nucleation center for silver particles upon the co-deposition of Ag and CeO$_2$ precursors. In addition, increased Ag 3d signal can be also associated with presence of Ag species smaller than 30 nm detected by XRD on the Ag-CeO$_2$/GO surface. XPS allows detecting photoelectrons emitted only from thin surface layer of 3–15 nm thick, and core atoms of large Ag particles do not contribute to XPS signal. More dispersed Ag species on the contrary may lead to enhanced and quantitative Ag 3d photoelectron yield.

To distinguish the Ag state in the Ag-containing catalysts, the Ag 3d and Ag MNN Auger regions were analyzed by recording high-resolution XPS spectra (Figure S3). The Auger parameters (AP) were calculated as:

$$\text{AP} = \text{Ag } 3d_{5/2} \text{ BE} + \text{Ag } M_5N_{45}N_{45} \text{ KE} \tag{1}$$

$$\text{or AP}' = \text{Ag } 3d_{5/2} \text{ BE} + \text{Ag } M_4N_{45}N_{45} \text{ KE} \tag{2}$$

where Ag $3d_{5/2}$ BE is the binding energy of the Ag $3d_{5/2}$ peak and Ag $M_5N_{45}N_{45}$ KE and Ag $M_4N_{45}N_{45}$ KE are kinetic energies of Auger electrons. The obtained AP values (718.4 and 720.3 eV for Ag/GO, 718.6 and 720.5 eV for Ag-CeO$_2$/GO) and AP′ values (724.3 and 726.0 eV for Ag/GO, 723.4 and 726.3 eV for Ag-CeO$_2$/GO) indicate the presence of both Ag(I) and Ag^0 species, respectively [49]. It is noteworthy that the contribution of the Ag^0 signal to the Ag MNN Auger region decreases from Ag/GO to Ag-CeO$_2$/GO, which can

be associated with a stronger junction between Ag and CeO_2 than the one between Ag and GO. The strong junction between Ag and CeO_2 is also facilitated by the redox reaction between the co-precipitated Ag^+ and Ce^{3+} precursors at the synthesis stage.

Thus, the structure of the support undergoes changes during the preparation of Ag- and/or CeO_2-containing catalysts. Stabilizing properties of ceria were revealed: a quantitative Ag deposition is observed during the co-deposition of silver and cerium oxide due to a stronger interaction with CeO_2 than with GO, which contributes to an increase in the active metal surface and particle dispersion and a developed Ag-CeO_2 interface.

2.2.3. TGA

The thermal stability of the synthesized catalysts was studied by thermogravimetric analysis. Figure 4 shows the TG (a) and DSC (b) data in the temperature range of 25–900 °C. Unlike the pristine support, the weight loss attributed to the dehydration decreases from 15 to 7–10 wt.% below 145 °C for the catalysts. Despite similar drying conditions, the amount of adsorbed water reduces, which indicates a more hydrophobic character of the catalysts. For all catalyst samples (in both oxidizing and inert atmospheres), a weight loss associated with the decarboxylation process is observed from 90 to 80 wt.%, and the maximum of the process shifts from 232 to 194 °C (Figure 4b). First, the smaller weight loss also indicates partial reduction of GO during the synthesis of catalysts observed by XPS (the support has an intermediate state between GO and rGO). The lower number of oxidized moieties is consistent with the decreased amount of adsorbed water in the catalysts in contrast to pristine GO. Second, the wedging action of Ag and CeO_2 nanoparticles reduces thermal stability due to the increase in structure defectiveness. These data are consistent with XRD results.

The amount of applied active components can be also estimated by the value of the residual mass in the air environment (Figure 4a). For the CeO_2/GO and Ag-CeO_2/GO catalysts, the residual masses are 12.5 and 18 wt.%, respectively, which is close to the corresponding calculated values of 10 and 15 wt.% and indicates the quantitative deposition of the active components. A slight increase in the experimental values can be associated with the presence of a graphite phase in the support, which exhibits high thermal stability (even in an oxidizing environment; Figure 2a). For the Ag/GO sample, the residual mass is 5.4 wt.%, which is slightly higher than that for the GO sample (4.2 wt.%). This may indicate that most of the residual mass is the graphite phase, while the silver content is substantially less than the expected 5 wt.%. These data correlate with XPS results.

The ceria-containing catalysts exhibit a significant shift in the combustion region of the support to lower temperatures of up to 250–650 °C (Figure 4b). The catalysis of GO combustion by CeO_2 particles is due to the oxidative activity of the lattice oxygen of the cerium oxide structure (due to the Ce^{4+}/Ce^{3+} redox transition), the high mobility of oxygen vacancies in the re-oxidation cycle of Ce^{3+} to Ce^{4+} with a molecular oxygen [17], and the developed contact with GO. A shift in the GO combustion temperature is observed for the Ag/GO catalyst, which also indicates the catalytic role of Ag in graphene oxidation. Thus, the active components contribute to low-temperature GO combustion in an oxidizing medium due to both increased defectiveness of the GO structure and the catalytic role of Ag and CeO_2.

2.2.4. Raman Spectroscopy

Raman spectroscopy was performed to study the state of carbon layers of the support in the synthesized samples (Figure S4). All samples exhibit intense *G* and *D* bands, with maxima at 1600 and 1355 cm^{-1} that are attributed to the E_{2g} symmetry stretching vibrations of the graphite-like sp^2-hybridized carbon and the A_{1g} symmetry stretching vibrations of carbon layers, respectively [50]. In addition, the samples are characterized by the bands of the second-order (or double resonance) two-phonon vibration modes [51] *2D*, *D+G*, and *2D′* with maxima at 2700, 2930, and 3195 cm^{-1}, respectively.

The *D* band at ~1350 cm^{-1} is Raman-inactive for pristine graphene but can be observed where the symmetry is broken by the carbon matrix defects [52]. Therefore, the relative intensity (peak area) of the Raman *D* and *G* bands serves for a quantitative assessment of the structure defectiveness of GO in the samples. As can be seen from the intensity ratio I_D/I_G represented in Figure S4, the samples possess a high degree of structural defects of the graphene layers. The number of defects increases from GO (I_D/I_G = 1.50) to rGO (I_D/I_G = 1.57). At the same time, for the supported catalysts, the I_D/I_G ratio is higher than the one for pristine GO or rGO: I_D/I_G (Ag/GO) = 1.63, I_D/I_G (CeO$_2$/GO) = 1.70, I_D/I_G (Ag-CeO$_2$/GO) = 1.68. Thus, according to Raman results, the increase in the number of defects in the support structure is associated with both the reduction of GO and the bonding of Ag and CeO$_2$ nanoparticles with the support.

2.2.5. UV–VIS Spectrometry

The optical properties of the synthesized catalysts and support were studied by electron (UV–VIS) spectrometry. Figure 5a shows the absorption spectra of aqueous suspensions of silver- and/or ceria-containing catalysts and graphene derivatives (GO and rGO) prepared by the US-mediated suspending of the sample for 15 min (sample concentration in the suspension is 0.75 g/L). The spectrum for the GO suspension is characterized by an intensive absorption peak, with a maximum at 226 nm and a shoulder at 304 nm, which correspond to the $\pi \rightarrow \pi^*$ electron transition of the C=C bonds and to the $n \rightarrow \pi^*$ transition of the C=O bonds, respectively [53]. When GO is reduced to rGO, the maximum of the $\pi \rightarrow \pi^*$ transition shifts from 226 to 257 nm, and the band related to the $n \rightarrow \pi^*$ transition disappears [34]. Hence, a decrease in the GO oxidation state leads to the band gap shrinking ($\pi \rightarrow \pi^*$ transition) [35,36].

A shift of the $\pi \rightarrow \pi^*$ transition maximum to 235, 244, and 252 nm is also observed for CeO$_2$/GO, Ag/GO, and Ag-CeO$_2$/GO, respectively. The maximal values are intermediate between those for GO and rGO, indicating a partial reduction of the support, which is consistent with the XRD, XPS, and TGA results. A slight broadening of the peak with a shoulder at ~325 nm indicates the absorption by CeO$_2$ particles for the CeO$_2$/GO and Ag-CeO$_2$/GO samples [45].

The Ag-CeO$_2$/GO sample was used to study the change in the catalyst state in a reducing medium in which the catalytic experiment took place. The absorption spectra for the Ag-CeO$_2$/GO suspension were recorded with a uniform NaBH$_4$ dosage once every 3 min with constant stirring in the cell (Figure 5b). With an increase in the reducing agent concentration to ~0.01 M, the position of the maximum of the $\pi \rightarrow \pi^*$ transition remains almost intact. At the same time, the appearance and intensity growth of the absorption peak with a maximum at ~380 nm is observed, which is attributed to silver surface plasmon resonance absorption (Ag SPR) [26,54]. Hence, in the as-prepared silver-containing samples, there are both the metallic state of silver recorded by XRD and also the surface-oxidized Ag species (AgO$_x$) recorded by XPS, which will be reduced to a metallic state under reductive conditions during the catalytic process.

Optical properties were also studied for the pre-reduced sample suspensions prepared by the optimized pre-reduction procedure (the US-mediated suspending of samples in 0.01 M NaBH$_4$ solution for 15 min; Figure S6). Figure 5c shows the UV–VIS spectra for the pre-reduced suspensions. The pre-reduced suspensions are distinguished by sedimentation stability and high optical density with a lower sample amount in the suspension (C(sample) = 0.15 g/L), which indicates better dispersion under the combined action of US treatment and the reducing agent. Insignificant changes in the GO (red.) spectrum are observed (a small shift of the maximum from 226 to 232 nm) due to the denser carbon structure that is partially accessible for reduction.
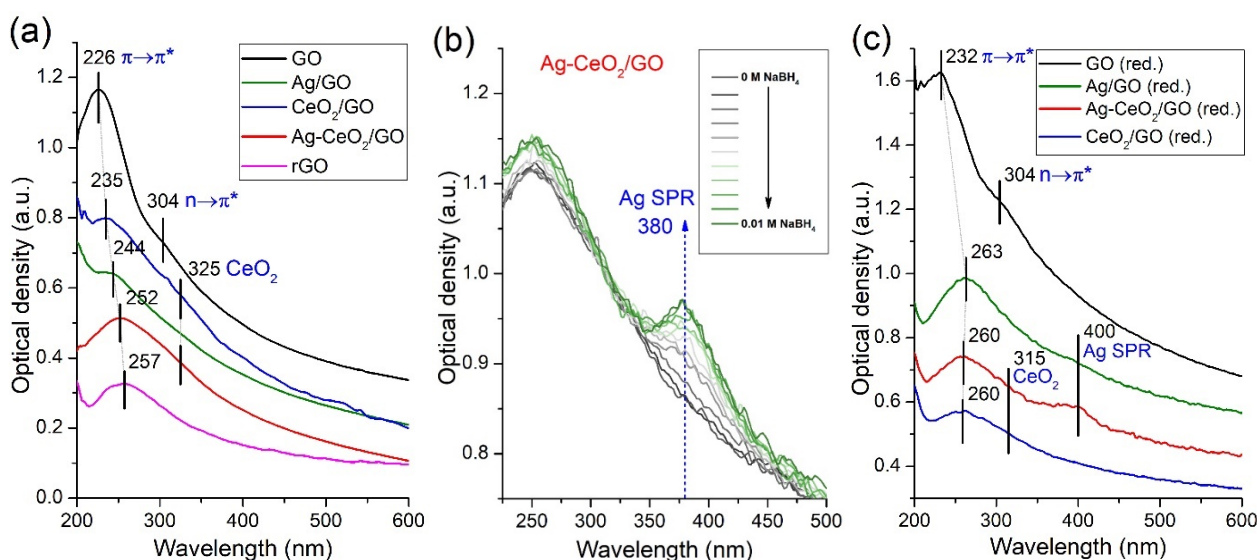
Figure 5. UV–VIS spectra of aqueous suspensions of graphene derivatives and catalysts (C(sample) = 0.75 g/L) (**a**); absorption spectra evolution of the Ag-CeO$_2$/GO suspension with increasing NaBH$_4$ concentration (**b**); and UV–VIS spectra of aqueous suspensions of graphene derivatives and catalysts (C(sample) = 0.15 g/L) pre-reduced in 0.01 M NaBH$_4$ in the presence of US for 15 min (**c**).

The spectra for the catalysts feature a close position of the maxima of the $\pi \rightarrow \pi^*$ transition at 260 nm, indicating support reduction in the presence of Ag and CeO$_2$ (reductant spillover) or due to the higher defectiveness that was shown by XRD and TG-DSC. In addition, for the Ag-CeO$_2$/GO (red.) sample, the Ag SPR absorption band is observed at 400 nm, while this band is quite low-intensive for the Ag/GO (red.) sample. This can be caused by a low Ag content in the Ag/GO (red.) catalyst, which is consistent with the XPS and TGA data. The difference in the SPR maxima position for the Ag-CeO$_2$/GO catalyst after reduction (400 nm) and during reduction (380 nm) is due to the fact that the SPR absorption band position is affected by the dielectric constant of the medium. There is intensive sorption of the nucleophilic reducing agent (NaBH$_4$) on the silver particle surface, followed by electron injection on the surface during the reduction of the AgO$_x$ species. As a result of enhanced electron density on the Ag particles, a blue shift of SPR absorption occurs [16]. In the spectra obtained after the suspension reduction, the SPR maximum has a characteristic position at 400 nm due to equalization of the excess electron density in the system after the reduction process and consumption of the reducing agent.

Thus, the study of optical properties allows judging on the oxidation state of graphene derivatives as well as the electrically conductive properties of the support by the value of the band gap (the position of the maximum of the $\pi \rightarrow \pi^*$ transition). The UV–VIS spectra make it possible to identify the Ag state in the silver-containing catalysts: oxidized Ag species occur and will be reduced to a metallic state during the catalysis process. Moreover, the presence or absence of silver particles in a particular system can be concluded according to the SPR absorption band provided by a sufficient amount of a reducing agent.

2.3. Catalytic Experiment

The catalytic properties of the synthesized silver- and/or ceria-containing catalysts were studied in 4-NP's reduction to 4-AP with sodium borohydride NaBH$_4$ in an aqueous medium at room temperature and ambient pressure (Figure 6).
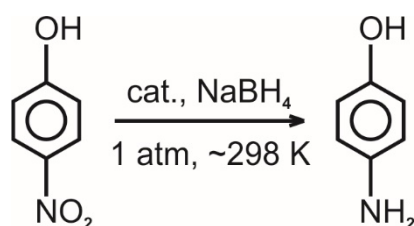
Figure 6. Schematic representation of the studied catalytic reaction.

The reaction was monitored using the UV-vis spectrometry of the solution in which the reaction proceeds (features of the experiment are presented in the Supplementary Materials). The intensity of the absorption peak of 4-NP at 400 nm decreases and a new peak of 4-AP absorption appears at 300 nm (Figure S5) during the catalytic reaction.

2.3.1. Activity of As-prepared Catalysts

The kinetic curves of 4-NP reduction for the synthesized samples were obtained (Figure 7a). Introducing the catalyst suspension into the solution containing 4-NP and $NaBH_4$ was considered the reaction start. Despite the possibility of the 4-NP reaction with sodium borohydride in terms of thermodynamics (E_0(4-NP/4-AP) = −0.76 V, E_0($NaBO_2$/$NaBH_4$) = −1.33 V), the reaction does not proceed in the absence of a catalyst. The extremely high activation barrier is due to the electrostatic repulsion of the 4-nitrophenolate ion and the BH_4^- anion [55]. The pristine GO support and the CeO_2/GO sample show no catalytic activity in this reaction (black and blue curves in Figure 7a, respectively).
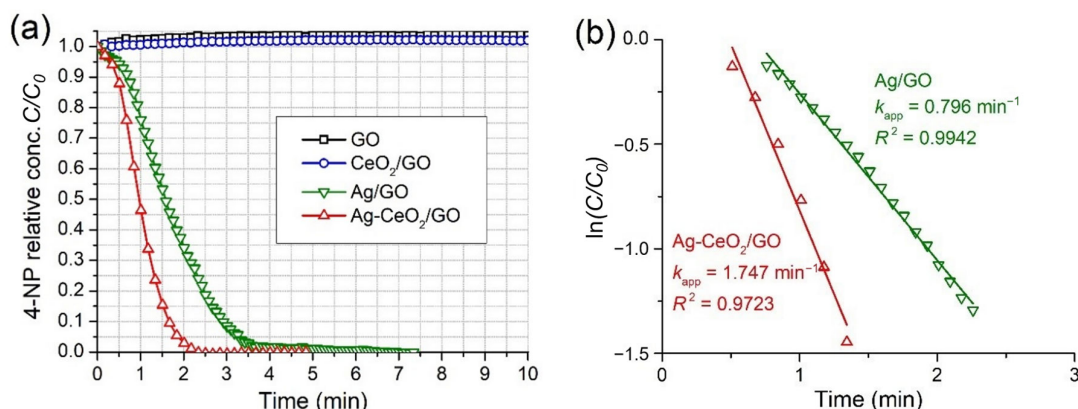

Figure 7. Kinetic curves of 4-NP reduction over the as-prepared samples (**a**) and the pseudo-first-order plot of the 4-NP relative concentration logarithm $\ln(C/C_0)$ versus the reaction time for the Ag/GO and Ag-CeO_2/GO catalysts (**b**). Experimental conditions: C(4-NP) = 7.5 × 10^{-5} M, C($NaBH_4$) = 0.015 M, C(catalyst) = 0.03 g/L, T = 297 K.

Silver-containing samples (Ag/GO and Ag-CeO_2/GO) exhibit substantial activity: the complete 4-NP conversion occurs in 4 and 2.5 min, respectively. Thus, the metal particles play a key role in the reduction process. The initial segment of the curves has a smaller slope (induction period) associated with the ongoing reduction of the oxidized silver species by sodium borohydride [16,56–58], the presence of which was shown by XPS and UV–VIS spectrometry of the catalyst suspensions (Figure 5b). That is, the surface-oxidized silver species AgO_x do not catalyze the reaction, and the active surface for this reaction is the metallic silver surface that gradually increases when the catalyst contacts the reducing medium (the reaction rate increases). The Ag-CeO_2/GO catalyst exhibits the highest activity due to the interaction of the co-deposited Ag and CeO_2 particles. The stabilization of a larger amount of silver (larger active surface) on the GO support in the presence of CeO_2 is consistent with the data on the residual masses in the TGA, XPS, and UV–VIS spectra.

For the Ag/GO and Ag-CeO$_2$/GO samples, the apparent rate constants were calculated within the pseudo-first-order reaction approximation [24] due to the large excess of the reducing agent in the system. The reaction rate depends on the 4-NP concentration according to the equation:

$$w = -k_{app}C \tag{3}$$

$$k_{app} = -\frac{\ln(C/C_0)}{t} \tag{4}$$

where w is the reaction rate (mol/L·min), k_{app} is the apparent rate constant (min^{-1}), C is the current 4-NP concentration (mol/L), and C_0 is the initial 4-NP concentration (mol/L). The rate constants were determined from the slope on the plot of the 4-NP relative concentration logarithm $\ln(C/C_0)$ versus the reaction time (Figure 7b). The obtained values of the apparent rate constants are 0.796 and 1.747 min^{-1} for Ag/GO and Ag-CeO$_2$/GO, respectively. The drafted dependencies have good linear fitting within the framework of this model, which emphasizes the model applicability in this process.

One of the key kinetic parameters characterizing the chemical transformation process is the activation energy value E_a that shows the temperature effect on the reaction rate. To study the temperature effect on the 4-NP reduction rate over the Ag-CeO$_2$/GO catalyst, the catalytic experiments were carried out by varying the temperature from 27 to 40 °C (300–313 K), with other conditions remaining unchanged. Figure 8a shows the plot of the 4-NP relative concentration logarithm $\ln(C/C_0)$ versus the reaction time at different temperatures. A regular increase in the slope value (pseudo-first-order reaction rate constant) is observed as the temperature increases. The chemical reaction temperature dependence obeys the Arrhenius equation:

$$\ln(k) = \ln(A) - \frac{E_a}{RT} \tag{5}$$

where $\ln(k)$ is the logarithm of the rate constant, $\ln(A)$ is the logarithm of the pre-exponential factor, E_a is the activation energy (kJ/mol), and R is the universal gas constant. The activation energy value was determined from the slope of the Arrhenius plot of ($\ln(k)$ versus $1000/T$; Figure 8b). The resulting E_a value is 72.9 kJ/mol. For silver-containing catalysts described in the literature, the activation energy of 4-NP reduction varies in the range of 8–42 kJ/mol [59]. However, as shown in [60], the E_a value for this reaction proceeding over the Ag@CeO$_2$ catalyst is 84.7 kJ/mol, which is close to the one obtained in this work. Thus, it can be concluded that the E_a value significantly depends on the composition and structure of the catalysts, and the catalytic reaction proceeding over the Ag-CeO$_2$ system is more sensitive to the temperature changes. In addition, the obtained E_a value is a reliable indicator of the reaction kinetic mode since the diffusion mode has a significantly lower activation energy (or temperature coefficient).
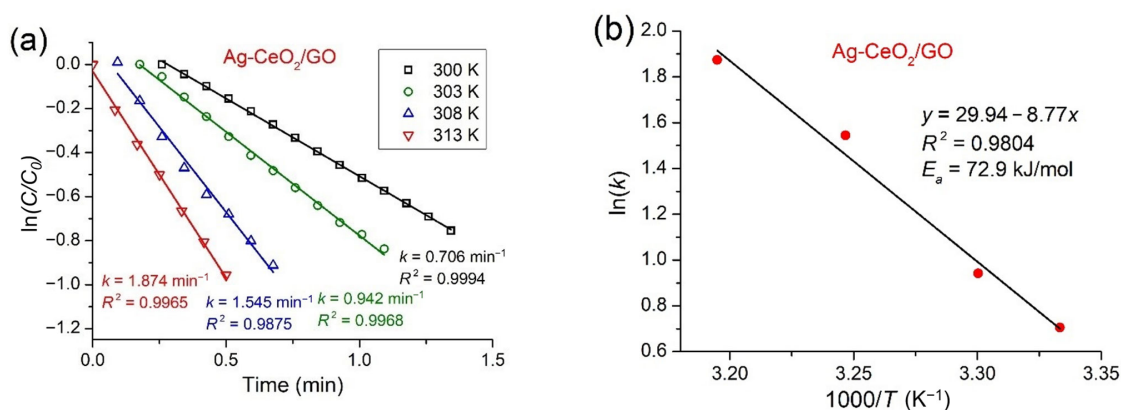

Figure 8. Plot of the 4-NP relative concentration logarithm $\ln(C/C_0)$ versus the reaction time at different temperatures (**a**) and Arrhenius plot of $\ln(k)$ versus $1000/T$ (**b**) for the Ag-CeO$_2$/GO catalysts. Experimental conditions: C(4-NP) = 7.5 × 10^{-5} M, C(NaBH$_4$) = 0.015 M, C(catalyst) = 0.015 g/L.

2.3.2. Pre-Reduced Catalysts

Since the state of the catalyst changes during the reaction (reduction of AgO_x surface species), the catalytic properties were also investigated for a series of pre-reduced catalyst samples. The catalyst pre-reduction condition was optimized (see Supplementary Materials) by simultaneous exposure to 0.01 M $NaBH_4$ and ultrasonic (US) treatment for 15 min to obtain catalyst suspensions with superior activity (Figure S6). Catalytic experiments were carried out in a similar manner with the pre-reduced samples. Figure 9a shows kinetic curves for the pre-reduced samples. GO (red.) and CeO_2/GO (red.) show no catalytic activity, as well as as-prepared samples. Silver-containing samples (Ag/GO (red.) and Ag-CeO_2/GO (red.)) show noticeable activity: complete 4-NP conversion occurs in 2.5 and 1.25 min, respectively. The rate constants were determined from the slope of the pseudo-first-order plot of the 4-NP relative concentration logarithm $\ln(C/C_0)$ versus the reaction time (Figure 9b). The calculated rate constant values are 1.615 and 3.674 min^{-1} for Ag/GO (red.) and Ag-CeO_2/GO (red.), respectively. Thus, the catalytic activity increases approximately twice for the silver-containing pre-reduced samples in comparison with the as-prepared ones.
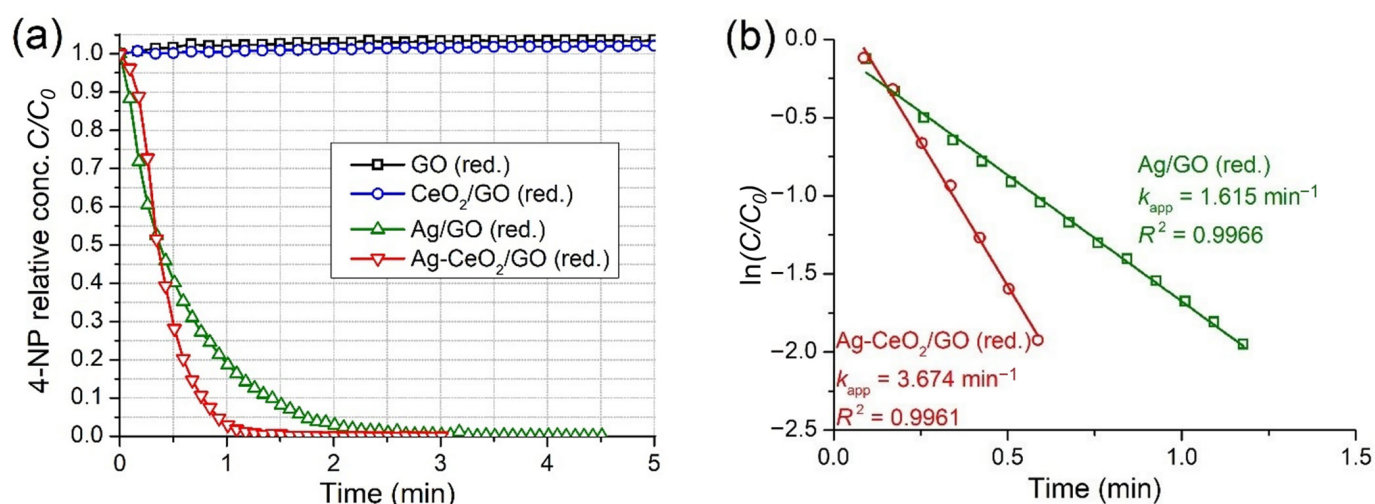

Figure 9. Kinetic curves of 4-NP reduction over the pre-reduced samples (**a**) and the pseudo-first-order plot of the 4-NP relative concentration logarithm $\ln(C/C_0)$ versus the reaction time for the Ag/GO (red.) and Ag-CeO_2/GO (red.) catalysts (**b**). Experimental conditions: C(4-NP) = 7.5 × 10^{-5} M, C($NaBH_4$) = 0.015 M, C(catalyst) = 0.03 g/L, T = 297 K.

The catalyst suspensions feature a high optical density, which was shown by UV–VIS spectrometry (Figure 5c), and sedimentation stability. That is, more efficient catalyst dispersing occurs under the combined action of US treatment and the reducing agent. Hence, the substantial increase in catalytic activity is due to the developed active surface, which is formed with the catalyst particle dispersing: silver particles encapsulated between the GO layers and "stacks" become available for the reagents.

The efficiency of the catalysts obtained in this work was assessed by comparing the activity (reaction rate constants) with the results obtained by other authors for some silver-containing catalysts used in the 4-NP-to-4-AP reduction with $NaBH_4$ under mild conditions (1 atm, ~25 °C). Table 4 summarizes the catalytic data.

Table 4. Data of catalytic experiments for 4-NP-to-4-AP reduction with $NaBH_4$ at atmospheric pressure and room temperature in an aqueous medium (C(catalyst) is the catalyst concentration in the reaction mixture, and k_{rel} is the relative rate constant: $k_{rel} = k_{app}/C$(catalyst)).

Catalyst	$C(NaBH_4)$ (mM)	C(4-NP) (mM)	C(catalyst) (g/L)	k_{app} (min^{-1})	k_{rel} (L/g·min)	Ref.
Ag/GO	15.0	0.075	0.030	0.796	26.5	
Ag-CeO$_2$/GO	15.0	0.075	0.030	1.747	58.2	This work
Ag/GO (red.)	15.0	0.075	0.030	1.615	53.8	
Ag-CeO$_2$/GO (red.)	15.0	0.075	0.030	3.674	122.5	
RGO/Ag/CeO$_2$-3	15.0	0.075	-	0.269	-	[37]
Ag-CeO$_2$/SBA-15	15.0	0.150	0.060	0.960	16.0	[24]
Ag@CeO$_2$	20.0	0.130	0.010	1.920	192.0	[60]
10Ag/CeO$_2$	15.0	0.150	0.120	3.793	31.6	[61]
1Pt1Ag/CeO$_2$	6.0	0.030	0.200	1.403	7.0	[62]
Ag$_{80}$Ni$_{20}$@CeO$_2$	10.0	0.080	0.400	6.231	15.6	[63]
Au-Ag-γ-Fe$_2$O$_3$/rGO	10.0	0.093	0.010	0.798	79.8	[64]
GO/Ag-Fe$_3$O$_4$	6.7	0.100	0.033	1.602	48.5	[65]
Ag-Fe$_3$O$_4$/RGO	100.0	0.100	1.600	2.640	1.7	[66]
Ag/MR-3	62.5	0.125	0.020	1.902	95.1	[59]
Ag-Pt (9:1)	0.6	0.100	0.0014	3.540	2528.6	[67]
Ag@hm-SiO$_2$	2.0	0.016	0.010	1.080	108.0	[68]
Ag-SiO$_2$	32.0	0.216	0.010	1.068	106.8	[69]
Ag-SiO$_2$	120.0	2.000	0.200	1.020	5.1	[70]
Ag/Triton X-705/SiNPs	100.0	0.100	2.400	3.636	1.5	[71]
NrGO1-Ag1-Gly5	0.4	0.085	0.172	0.426	2.5	[72]
Ag NPs@MOF-199 s/CCFs	10.0	0.100	0.002	0.149	74.4	[73]
Fe$_3$O$_4$@MIL-100(Fe)/Ag	38.7	0.096	0.032	2.830	87.7	[74]
Ag@NOTT-300(Al)	100.0	0.144	0.100	2.670	26.7	[75]

The results show that the synthesized catalysts possess high catalytic activity, which is comparable to that of a number of catalysts for 4-NP reduction and in some cases exceeding it. First, one of the factors of such high activity of Ag-CeO$_2$/GO is the developed active surface accessible for the reaction. In addition, the charged states of the catalyst components at the Ag-CeO$_2$ and Ag-GO interfaces can be favorable for sorption of the 4-nitrophenolate ion and the BH$_4^-$ anion [55]. Moreover, GO exhibits better sorption properties toward nitroaromatic compounds due to the π–π stacking interaction of the 4-NP aromatic ring with the sp^2-hybridized carbon material [37]. In addition, the negative zeta potential of the GO surface promotes the implementation of the "pull-push" mechanism [59]. This implies electrostatic attraction of the electrophilic 4-NP and repulsion of the nucleophilic 4-AP that also affects the more rapid course of the reaction. Therefore, the combination of factors has a positive effect on the Ag-CeO$_2$/GO catalytic activity.

Thus, 4-NP reduction at room temperature and atmospheric pressure in an aqueous medium shows that Ag-CeO$_2$/GO catalysts are promising effective systems in NCs' reduction into corresponding ACs.

2.3.3. Stability and Leaching Tests

Not only the activity value in a single conversion cycle but also the ability to maintain the required activity over time are important for the practical use of a catalyst. The stability of the as-prepared Ag-CeO$_2$/GO catalyst was evaluated by recording the kinetic data of 4-NP reduction upon a periodic reaction renewal. Figure 10a shows the kinetic curves of the Ag-CeO$_2$/GO sample obtained by dosing the reagents at a certain time interval. The kinetic curves show no inflections at the initial curve segment after the completion of the first conversion cycle, which indicates the reduction of the oxidized silver particle surface. In addition, starting from the fifth cycle, there is a certain increase in the 4-NP complete conversion time up to ~7.5 min for the seventh cycle: the reaction rate slows down from cycle to cycle at conversion values above 50%.
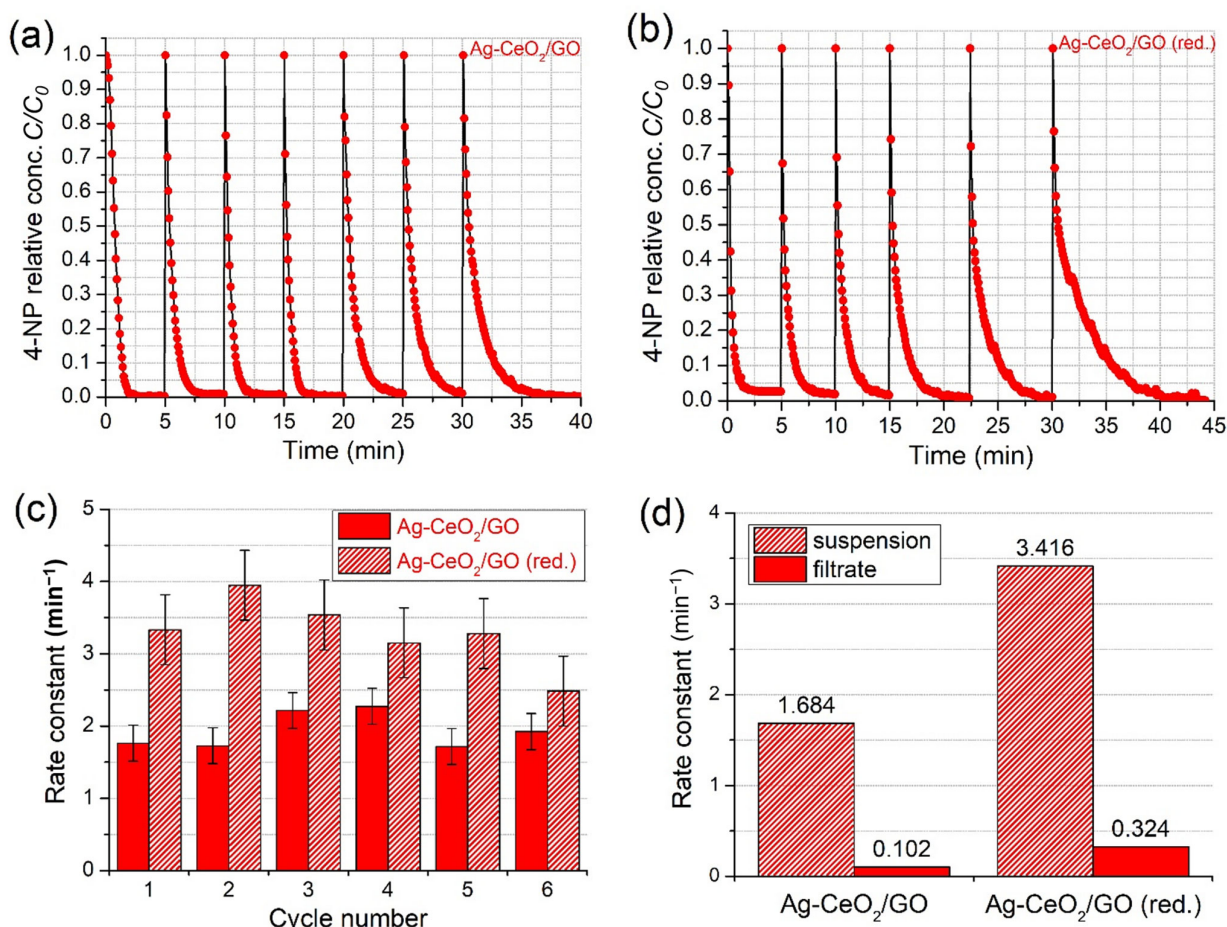
Figure 10. As-prepared Ag-CeO$_2$/GO (**a**) and pre-reduced Ag-CeO$_2$/GO (red.) (**b**) kinetic curves and the corresponding rate constant values of 4-NP reduction consecutive cycles (**c**); rate constant values of 4-NP reduction with Ag-CeO$_2$/GO and Ag-CeO$_2$/GO (red.) suspensions and their filtrates (**d**). Experimental conditions: C(4-NP) = 7.5 × 10^{-5} M, C(NaBH$_4$) = 0.015 M, C(catalyst) = 0.03 g/L, T = 297 K.

The stability of the pre-reduced Ag-CeO$_2$/GO (red.) catalyst was also studied by recording the kinetic data of 4-NP reduction upon periodic reaction renewal (Figure 10b). Similarly to the as-prepared Ag-CeO$_2$/GO catalyst, there are no inflections at the initial curve segment in each reaction cycle, which indicates complete reduction of the oxidized surface of silver particles in the prepared suspension. Starting from the second cycle, there is a certain increase in the 4-NP complete conversion time up to ~10 min in the sixth cycle. The conversion time increases more dramatically than for the as-prepared Ag-CeO$_2$/GO catalyst from cycle to cycle at conversion values greater than 50%.

The chemical transformation kinetics of NC reduction by NaBH$_4$ proceeds according to the Langmuir–Hinshelwood model [57,58,63]. First, NC and NaBH$_4$ are adsorbed on the active sites of the metallic catalyst surface. NaBH$_4$ undergoes the hydrolysis process in the presence of the catalyst via B–H bond cleavage, followed by adsorbed atomic hydrogen formation and electron injection into the metal particle [76]. Next, the active hydrogen species interact with the nitro group in the NC molecule, and the reaction proceeds until the reduction is completed by 4-AP desorption. The excessive electrons formed on the metal particle can also reduce the nitro group regarding the electron transfer process from the particle to the adsorbed substrate [77]. However, the hydrogen evolution reaction is a competitive process caused by the high coverage of the metal surface with the active hydrogen species and excessive electron density, which proceeds according to either the Heyrovsky or the Tafel model [67]. The hydrogen evolution has a higher rate in contrast to 4-NP reduction, which implies intensive NaBH$_4$ conversion and accumulation of hydrolysis

products. As shown in Figure S6, prolonged contact of the catalyst with $NaBH_4$ solution of a high concentration leads to a substantial reaction rate decrease. Hence, the competitive sorption of 4-NP and $NaBH_4$ hydrolysis products deactivates/passivates the catalyst occupying the sorption sites on the active surface. This causes the reaction rate to slow down from cycle to cycle at conversion values greater than 50% and the conversion time to increase for the target reaction. Moreover, since the pre-reduced catalyst possesses higher activity, the $NaBH_4$ conversion and accumulation of hydrolysis products are more intensive. Thus, greater competitive sorption of 4-NP and conversion products and catalyst deactivation/passivation occur, resulting in a dramatic increase in conversion time from cycle to cycle for the pre-reduced catalyst.

Figure 10c shows a bar chart for the apparent rate constants, k_{app}, obtained in 4-NP reduction cycles on the as-prepared $Ag-CeO_2/GO$ and pre-reduced $Ag-CeO_2/GO$ (red.) catalysts, which are calculated within the pseudo-first-order approximation at conversion values less than 50%. The catalysts show good stability, maintaining stable activity, i.e., k_{app} of ~1.7 min^{-1} over six conversion cycles and k_{app} of ~3.25 min^{-1} over five conversion cycles. A slight increase in the rate constants for $Ag-CeO_2/GO$ in the third and fourth cycles and $Ag-CeO_2/GO$ (red.) in the second cycle may be associated with a deeper reduction of the oxidized silver surface after a certain time, which leads to the active surface and, consequently, the reaction rate increasing.

Since the 4-NP reduction reaction occurs in the solution, active component leaching can take place. The degree of the active component loss can affect catalyst reusage. The leaching of active components was studied, with the 4-NP reduction catalyzed by either freshly prepared $Ag-CeO_2/GO$ and $Ag-CeO_2/GO$ (red.) suspensions or solutions obtained by the suspension filtration. Figure 10d shows a bar chart of the apparent rate constants k_{app} for 4-NP reduction catalyzed by both the as-prepared $Ag-CeO_2/GO$ and pre-reduced $Ag-CeO_2/GO$ (red.) catalyst suspensions and their filtrates. According to the data, only ~6 and 9.5% of the $Ag-CeO_2/GO$ and $Ag-CeO_2/GO$ (red.) catalyst activities come from the leached species of the active component. Thus, the $Ag-CeO_2/GO$ catalysts demonstrate both significant catalytic stability and a low leaching degree of the active components. The $Ag-CeO_2/GO$ catalysts are effective systems for NCs' reduction into corresponding ACs.

3. Materials and Methods

3.1. Synthesis of Graphene Oxide

Graphene oxide (GO) is synthesized by oxidative treatment of graphite according to the modified Hummers method [78]. The features of the GO synthesis are presented in the Supplementary Materials. The final product was dried under vacuum for 48 h at 60 °C to obtain graphene oxide (GO).

Reduced graphene oxide (rGO) was prepared from the synthesized GO and was used as a reference sample. Briefly, 1 g of GO was suspended in 500 mL of water, and 10 g of solid $NaBH_4$ powder was added. The resulting mixture was constantly stirred for 24 h at 100 °C. Next, the mixture was filtered under vacuum, and the precipitate was washed with distilled water. The final product was dried under vacuum for 48 h at 60 °C.

3.2. Synthesis of Catalysts

Silver- and/or ceria-containing catalysts were synthesized by the deposition-precipitation method. To prepare 1 g of the catalyst, a certain mass of GO was introduced into 50 mL of water and subjected to ultrasonic (US) treatment for 10 min at room temperature (frequency = 40 kHz, power = 50 W). A 25% ammonia solution was added dropwise to the resulting suspension to shift the pH from 1 to 4–5. Next, the precursors of active components ($m(AgNO_3)$ = 0.0787 g and/or $m(Ce(NO_3)_3 \cdot 6H_2O)$ = 0.2524 g) were added, and the mixture was stirred for 10 min. After that, a precipitant (25% ammonia solution) was slowly added to a suspension to a pH of ~10. The resulting mixture was hydrothermally treated for 1 h at 95 °C in a Teflon autoclave. Further, the precipitate was dried in an air atmosphere for 4 h at 50 °C and then dried under vacuum for 48 h at 60 °C. The calculated amounts of silver and cerium (IV) oxide in the

obtained samples were 5 and 10 wt.%, respectively. The samples were named as Ag/GO (ω(Ag) = 5 wt.%), CeO_2/GO (ω(CeO_2) = 10 wt.%), and Ag-CeO_2/GO (ω(Ag) = 5 wt.%, ω(CeO_2) = 10 wt.%).

3.3. Characterization of Samples

The porous structure of the samples was characterized by low-temperature nitrogen adsorption-desorption at −196 °C (77 K) with a 3Flex automatic gas sorption analyzer (Micromeritics, Norcross, GA, USA). The specific surface area was determined using the multipoint BET method by analyzing the adsorption isotherm in the P/P_o range from 0.05 to 0.20. To plot the size distribution of mesopores, the BJH-adsorption method was used with the analysis of the adsorption branch of the nitrogen adsorption-desorption isotherms. The Horvath–Kawazoe method was used to construct the size distribution of micropores. Before the measurements, 20–25 mg of the milled samples was degassed under vacuum at 200 °C for 2 h.

The phase composition of the support and catalysts was studied by powder X-ray diffraction (XRD). XRD data were obtained using a MiniFlex 600 diffractometer (Rigaku, Tokyo, Japan) with CuK_α radiation (λ = 1.5418 Å) in the 2θ diffraction angle range from 5° to 70° with a recording rate of 2°/min and a step of 0.02°. The particle size was calculated according to the Scherrer equation:

$$D = \frac{K\lambda}{\beta \cos \theta} \tag{6}$$

where D is the average particle size, K is the Scherrer constant (0.89), λ is the X-ray radiation wavelength, β is the full width at half maximum (FWHM), and θ is the scattering angle (diffraction peak maximum). From the Scherrer equation, the number of GO layers was calculated using the equation:

$$N = \frac{D_{002}}{d_{002}} \tag{7}$$

where N is the number of GO layers, D_{002} is the thickness of the GO crystallite, and d_{002} is the GO interlayer distance.

The elemental composition and surface chemical state of the samples were analyzed by X-ray photoelectron spectroscopy (XPS) using the K-Alpha Nexsa superhigh-vacuum X-ray photoelectron spectrometer (Thermo Fisher Scientific, Waltham, MA, USA). The survey and high-resolution XPS spectra of a 200-μm^2 surface region were recorded with AlK_α radiation (1486.74 eV) as the X-ray source and a pass energy of 200 (a step of 1 eV) and 50 (a step of 0.1 eV) eV, respectively. The base pressure in the analysis chamber was 10^{-9} mbar. A flood gun was used for charge compensation. The obtained spectra were analyzed using Avantage Thermo Fisher and Casa XPS software.

The thermal properties of the samples were investigated by thermogravimetric analysis (TGA) in TG-DSC mode with mass spectra detection. The survey was carried out using the STA 449 F1 Jupiter instrument with a QMS 403 D Aeolos mass spectrometer (Netzsch, Selb, Germany) in an oxidizing (air) or an inert (argon) atmosphere in a temperature range from 25 to 900 °C with a heating rate of 10 °C/min.

The structure state of the carbon matrix in the support and catalysts was studied by Raman spectroscopy using an inVia Raman confocal microscope (Renishaw, Wotton-Under-Edge, UK) under standard conditions with monochromatic excitation radiation at a wavelength of 532 nm.

The optical properties of the samples were investigated by electron (UV–VIS) spectrometry. The UV–VIS absorption spectra of the aqueous suspensions of the samples were recorded on a CM 2203 spectrofluorometer (SOLAR, Minsk, Belarus) in an in situ cell equipped with a quartz cuvette (10 mm optical path), a magnetic stirrer, and a thermostat, in a wavelength range of 200–600 nm. The suspensions were prepared by suspending the sample in distilled water using US treatment (frequency = 40 kHz, power = 50 W) for 15 min.

3.4. Catalytic Experiments

The catalytic properties of the synthesized samples were studied in 4-NP-to-4-AP reduction with sodium borohydride $NaBH_4$ at room temperature (~25 °C) and atmospheric pressure in an aqueous medium. The reaction was carried out in an in situ cell of the Solar CM 2203 spectrofluorometer equipped with a quartz cuvette (10 mm optical path), a magnetic stirrer, and a thermostat. Briefly, 1.25 mL of 1.5×10^{-5} M 4-NP solution and 0.75 mL of freshly prepared 0.05 M $NaBH_4$ solution were sequentially introduced into the cuvette (molar ratio 4-NP:$NaBH_4$ = 1:200). Next, a certain volume of water required to reach a total reaction mixture volume of 2.5 mL and 100 μL of 0.75 g/L catalyst suspension were added to the mixture. The catalyst suspension was prepared by suspending 3.75 mg of the sample in 5 mL of distilled water using US treatment (frequency = 40 kHz, power = 50 W) for 15 min. The final concentrations of the components in the initial reaction mixture were 7.5×10^{-5} M for 4-NP, 0.015 M for $NaBH_4$, and 0.03 g/L for the catalyst. The reaction was monitored by recording the absorption spectra of the resulting solution in a wavelength range of 200–600 nm. Kinetic data were obtained by spectrophotometric measurement of the optical density of the solution at a wavelength of 400 nm (absorption peak of the 4-nitrophenolate ion) with a frequency of 5 s and with constant stirring at 600 rpm and constant temperature. The catalyst addition into the reaction mixture containing 4-NP and $NaBH_4$ was considered the reaction start. The stability test of the catalysts was carried out by recording kinetic data upon a periodic renewal of the reagents in the solution by dosing 100 μL of a solution containing 2.25×10^{-3} M 4-NP and 0.225 M $NaBH_4$ with a certain time interval.

4. Conclusions

To sum up, graphene oxide (GO) was synthesized by the oxidative treatment of graphite according to the modified Hummers method. The synthesized support had a micro-mesoporous structure (pore volume of 0.1 cm^3/g) with an average micropore size of 0.45 nm and a mesopore size of 5.23 nm, as well as a developed specific surface area of 54.6 m^2/g with the main contribution of micropores (46 m^2/g). The structure was represented by microporous aggregates of folded turbostratic carbon layers ("stacks") 5 nm thick that were separated by mesopores.

The synthesis of silver- and/or ceria-containing catalysts based on GO was carried out by the deposition-precipitation method. The applied synthesis approaches allowed obtaining nanosized Ag and CeO_2 particles with sizes up to 30 and 5 nm in the GO structure. The particles were bonded to the carbon matrix and distorted/wedged GO. The GO matrix was partially reduced in the catalysts. The co-deposition of silver and cerium (IV) oxide onto graphene oxide was revealed to promote stabilization of a larger silver amount on the support and/or increase the Ag particle dispersion due to the stronger interaction of silver with CeO_2. The ceria surface acted as a nucleation center for Ag particles. The strong bonding of Ag and CeO_2 was also facilitated by the redox reaction between the precipitated Ag^+ and Ce^{3+} precursors at the synthesis stage.

The 4-nitrophenol (4-NP)-to-4-aminophenol (4-AP) reduction with sodium borohydride ($NaBH_4$) in an aqueous medium at atmospheric pressure and room temperature was investigated. The reaction was catalyzed by silver particles featuring a metallic surface state. $NaBH_4$ played a double role in this process: the reduction of the oxidized silver species AgO_x on the particle surface and 4-NP reduction. The Ag-CeO_2/GO catalyst demonstrated the highest activity in the synthesized series of catalysts that was due to the larger active surface in the presence of CeO_2 as a modifying agent. The catalytic activity increased for the pre-reduced catalysts prepared by US-mediated reductive treatment due to better dispersion of the catalyst in the suspension and a larger active surface of the freshly reduced metallic silver. The Ag-CeO_2/GO catalyst retained good stability in the 4-NP reduction reaction upon periodic reaction renewal and a low leaching degree of active components in the solution.

Thus, the combination of high activity and stability makes Ag-CeO$_2$/GO catalysts effective systems for the reduction of nitroaromatic compounds into their corresponding aromatic amines.

References

1. Ju, K.-S.; Parales, R.E. Nitroaromatic Compounds, from Synthesis to Biodegradation. *Microbiol. Mol. Biol. Rev.* **2010**, *74*, 250–272. [CrossRef] [PubMed]
2. Singh, D.; Mishra, K.; Ramanthan, G. Bioremediation of Nitroaromatic Compounds. In *Wastewater Treatment Engineering*; Samer, M., Ed.; IntechOpen: London, UK, 2015; pp. 51–83. [CrossRef]
3. Králik, M.; Turáková, M.; Mačák, I.; Lehocký, P. Aniline-catalysis and chemical engineering. In Proceedings of the 41st International Conference of Slovak Society of Chemical Engineering, Tatranské Matliare, Slovakia, 26–30 May 2014; pp. 723–733.
4. Saha, B.; De, S.; Dutta, S. Recent Advancements of Replacing Existing Aniline Production Process with Environmentally Friendly One-Pot Process: An Overview. *Crit. Rev. Env. Sci. Technol.* **2013**, *43*, 84–120. [CrossRef]
5. Couto, C.S.; Madeira, L.M.; Nunes, C.P.; Araújo, P. Commercial Catalysts Screening for Liquid Phase Nitrobenzene Hydrogenation. *Appl. Catal. A: Gen.* **2016**, *522*, 152–164. [CrossRef]
6. Fishbein, L. Aromatic Amines. In *Anthropogenic Compounds. The Handbook of Environmental Chemistry*; Hutzinger, O., Ed.; Springer: Berlin/Heidelberg, Germany, 1984; Volume 3/3C. [CrossRef]
7. Samer, M. Biological and Chemical Wastewater Treatment Processes. In *Wastewater Treatment Engineering*; Samer, M., Ed.; IntechOpen: London, UK, 2015; pp. 1–50. [CrossRef]
8. Kumar, B. Graphene- and Graphene Oxide-Bounded Metal Nanocomposite for Remediation of Organic Pollutants. In *Carbon-Based Material for Environmental Protection and Remediation*; Bartoli, M., Frediani, M., Rosi, L., Eds.; IntechOpen: London, UK, 2020. [CrossRef]
9. Zhang, K.; Suh, J.M.; Choi, J.-W.; Jang, H.W.; Shokouhimehr, M.; Varma, R.S. Recent Advances in the Nanocatalyst-Assisted NaBH$_4$ Reduction of Nitroaromatics in Water. *ACS Omega* **2019**, *4*, 483–495. [CrossRef] [PubMed]
10. Orlandi, M.; Brenna, D.; Harms, R.; Jost, S.; Benaglia, M. Recent Developments in the Reduction of Aromatic and Aliphatic Nitro Compounds to Amines. *Org. Process Res. Dev.* **2018**, *22*, 430–445. [CrossRef]
11. Zang, W.; Li, G.; Wang, L.; Zhang, X. Catalytic hydrogenation by noble-metal nanocrystals with well-defined facets: A review. *Catal. Sci. Technol.* **2015**, *5*, 2532–2553. [CrossRef]

12. Torbina, V.V.; Vodyankin, A.A.; Ten, S.; Mamontov, G.V.; Salaev, M.A.; Sobolev, V.I.; Vodyankina, O.V. Ag-Based Catalysts in Heterogeneous Selective Oxidation of Alcohols: A Review. *Catalysts* **2018**, *8*, 447. [CrossRef]

13. Vodyankina, O.V.; Mamontov, G.V.; Dutov, V.V.; Kharlamova, T.S.; Salaev, M.A. Ag-Containing Nanomaterials in Heterogeneous Catalysis: Advances and Recent Trends. In *Advanced Nanomaterials for Catalysis and Energy: Synthesis, Characterization and Applications*; Sadykov, V.A., Ed.; Elsevier: Amsterdam, The Netherlands, 2018; pp. 143–175. [CrossRef]

14. Wen, C.; Yin, A.; Dai, W.-L. Recent advances in silver-based heterogeneous catalysts for green chemistry processes. *Appl. Catal. B: Environ.* **2014**, *160–161*, 730–741. [CrossRef]

15. Liao, G.; Gong, Y.; Zhong, L.; Fang, J.; Zhang, L.; Xu, Z.; Gao, H.; Fang, B. Unlocking the door to highly efficient Ag-based nanoparticles catalysts for $NaBH_4$-assisted nitrophenol reduction. *Nano Res.* **2019**, *12*, 2407–2436. [CrossRef]

16. Pradhan, N.; Pal, A.; Pal, T. Silver nanoparticle catalyzed reduction of aromatic nitro compounds. *Colloids Surf. A: Physicochem. Eng. Aspects* **2002**, *196*, 247–257. [CrossRef]

17. Montini, T.; Melchionna, M.; Monai, M.; Fornasiero, P. Fundamentals and Catalytic Applications of CeO_2-Based Materials. *Chem. Rev.* **2016**, *116*, 5987–6041. [CrossRef] [PubMed]

18. Salaev, M.A.; Salaeva, A.A.; Kharlamova, T.S.; Mamontov, G.V. Pt–CeO_2-based composites in environmental catalysis: A review. *Appl. Catal. B: Environ.* **2021**, *295*, 120286. [CrossRef]

19. Grabchenko, M.V.; Mamontov, G.V.; Zaikovskii, V.I.; La Parola, V.; Liotta, L.F.; Vodyankina, O.V. The role of metal–support interaction in Ag/CeO_2 catalysts for CO and soot oxidation. *Appl. Catal. B: Environ.* **2020**, *260*, 118148. [CrossRef]

20. Kong, D.; Wang, G.; Pan, Y.; Hu, S.; Hou, J.; Pan, H.; Campbell, C.T.; Zhu, J. Growth, Structure, and Stability of Ag on CeO_2(111): Synchrotron Radiation Photoemission Studies. *J. Phys. Chem. C* **2011**, *115*, 6715–6725. [CrossRef]

21. Mamontov, G.V.; Grabchenko, M.V.; Sobolev, V.I.; Zaikovskii, V.I.; Vodyankina, O.V. Ethanol dehydrogenation over $Ag-CeO_2/SiO_2$ catalyst: Role of $Ag-CeO_2$ interface. *Appl. Catal. A: General* **2016**, *528*, 161–167. [CrossRef]

22. Mikheeva, N.N.; Zaikovskii, V.I.; Larichev, Y.V.; Mamontov, G.V. Toluene abatement on $Ag-CeO_2/SBA-15$ catalysts: Synergistic effect of silver and ceria. *Mater. Today Chem.* **2021**, *21*, 100530. [CrossRef]

23. Ou, C.-C.; Chen, C.-H.; Chan, T.-S.; Chen, C.-S.; Cheng, S. Influence of pretreatment on the catalytic performance of Ag/CeO_2 for formaldehyde removal at low temperature. *J. Catal.* **2019**, *380*, 43–54. [CrossRef]

24. Taratayko, A.; Larichev, Y.; Zaikovskii, V.; Mikheeva, N.; Mamontov, G. $Ag-CeO_2/SBA-15$ composite prepared from Pluronic P123@SBA-15 hybrid as catalyst for room-temperature reduction of 4-nitrophenol. *Catal. Today* **2021**, *375*, 576–584. [CrossRef]

25. Qian, X.; Kuwahara, Y.; Mori, K.; Yamashita, H. Silver Nanoparticles Supported on CeO_2-SBA-15 by Microwave Irradiation Possess Metal–Support Interactions and Enhanced Catalytic Activity. *Chem. Eur. J.* **2014**, *20*, 15746–15752. [CrossRef]

26. Verma, P.; Kuwahara, Y.; Mori, K.; Yamashita, H. Plasmonic catalysis of Ag nanoparticles deposited on CeO_2 modified mesoporous silica for the nitrostyrene reduction under light irradiation conditions. *Catal. Today* **2019**, *324*, 83–89. [CrossRef]

27. Geim, A.K.; Novoselov, K.S. The rise of graphene. *Nat. Mater.* **2007**, *6*, 183–191. [CrossRef] [PubMed]

28. Wang, X.; Chen, S. Graphene-Based Nanocomposites. In *Physics and Applications of Graphene–Experiments*; Mikhailov, S., Ed.; IntechOpen: London, UK, 2011; pp. 135–168. [CrossRef]

29. Obodo, R.M.; Ahmad, I.; Ezema, F.I. Introductory Chapter: Graphene and Its Applications. In *Graphene and Its Derivatives-Synthesis and Applications*; Ahmad, I., Ezema, F.I., Eds.; IntechOpen: London, UK, 2019. [CrossRef]

30. Yusuf, M.; Kumar, M.; Khan, M.A.; Sillanpa, M.; Arafat, H. A review on exfoliation, characterization, environmental and energy applications of graphene and graphene-based composites. *Adv. Colloid Interface Sci.* **2019**, *273*, 102036. [CrossRef]

31. Prasad, C.; Liu, Q.; Tang, H.; Yuvaraja, G.; Long, J.; Rammohan, A.; Zyryanov, G.V. An overview of graphene oxide supported semiconductors based photocatalysts: Properties, synthesis and photocatalytic applications. *J. Mol. Liq.* **2020**, *297*, 111826. [CrossRef]

32. Shen, Y.; Fang, Q.; Chen, B. Environmental Applications of Three-Dimensional Graphene-Based Macrostructures: Adsorption, Transformation, and Detection. *Environ. Sci. Technol.* **2014**, *49*, 67–84. [CrossRef]

33. Paramasivan, T.; Sivarajasekar, N.; Muthusaravanan, S.; Subashini, R.; Prakashmaran, J.; Sivamani, S.; Ajmal Koya, P. Graphene Family Materials for the Removal of Pesticides from Water. In *A New Generation Material Graphene: Applications in Water Technology*; Naushad, M., Ed.; Springer: Berlin, Germany, 2019; pp. 309–327. [CrossRef]

34. Jimenez-Cervantes, E.; López-Barroso, J.; Martínez-Hernández, A.L.; Velasco-Santos, C. Graphene-Based Materials Functionalization with Natural Polymeric Biomolecules. In *Recent Advances in Graphene Research*; Nayak, P.K., Ed.; IntechOpen: London, UK, 2016; pp. 257–298. [CrossRef]

35. Gemeay, A.; El-Halwagy, M. Immobilization Impact of Photocatalysts onto Graphene Oxide. In *Graphene Oxide-Applications and Opportunities*; Kamble, G., Ed.; IntechOpen: London, UK, 2018; pp. 107–126. [CrossRef]

36. Romero, U.A.M.; Soto, M.Á.V.; Jiménez, L.L.; Quintana, J.Á.; García, S.A.P. Graphene Derivatives: Controlled Properties, Nanocomposites, and Energy Harvesting Applications. In *Graphene Materials-Structure, Properties and Modifications*; Kyzas, G.Z., Mitropoulos, A., Eds.; IntechOpen: London, UK, 2017; pp. 77–96. [CrossRef]

37. Ji, Z.; Shen, X.; Yang, J.; Zhu, G.; Chen, K. A novel reduced graphene oxide/Ag/CeO_2 ternary nanocomposite: Green synthesis and catalytic properties. *Appl. Catal. B: Environ.* **2014**, *144*, 454–461. [CrossRef]

38. Wang, Y.; Lu, C.; Yin, Z. Reduced graphene oxide decorated with Ag/CeO_2 nanocomposite towards room temperature photocatalytic esterification of aldehydes. *Mater. Lett.* **2020**, *270*, 127723. [CrossRef]

39. Tao, X.; Zhou, Y.; Xu, K.; Wu, Y.; Mi, J.; Li, Y.; Liu, Q.; Cheng, X.; Zhao, N.; Shi, H.; et al. Bifunctional Material with Organic Pollutant Removing and Antimicrobial Properties: Graphene Aerogel Decorated with Highly Dispersed Ag and CeO₂ Nanoparticles. *ACS Sustainable Chem. Eng.* **2018**, *6*, 16907–16919. [CrossRef]

40. Mardani, C.; Rizal, M.Y.; Saleh, R.; Taufik, A.; Yin, S. Synthesis and characterization of Ag/CeO₂/graphene nanocomposites as catalysts for water-pollution treatment. *Appl. Surf. Sci.* **2020**, *530*, 147297. [CrossRef]

41. Thommes, M.; Kaneko, K.; Neimark, A.V.; Olivier, J.P.; Rodriguez-Reinoso, F.; Rouquerol, J.; Sing, K.S.W. Physisorption of gases, with special reference to the evaluation of surface area and pore size distribution (IUPAC Technical Report). *Pure Appl. Chem.* **2015**, *87*, 1051–1069. [CrossRef]

42. Huh, S.H. Thermal Reduction of Graphene Oxide. In *Physics and Applications of Graphene–Experiments*; Mikhailov, S., Ed.; IntechOpen: London, UK, 2011; pp. 73–90. [CrossRef]

43. Ossonon, B.D.; Bélanger, D. Synthesis and characterization of sulfophenyl-functionalized reduced graphene oxide sheet. *RSC Adv.* **2017**, *7*, 27224–27234. [CrossRef]

44. He, Y.; Zhang, N.; Wu, F.; Xu, F.; Liu, Y.; Gao, J. Graphene oxide foams and their excellent adsorption ability for acetone gas. *Mater. Res. Bull.* **2013**, *48*, 3553–3558. [CrossRef]

45. Verma, R.; Samdarshi, S.K. In-Situ Decorated Optimized CeO₂ on Reduced Graphene Oxide with Enhanced Adsorptivity and Visible Light Photocatalytic Stability and Reusability. *J. Phys. Chem. C* **2016**, *120*, 22281–22290. [CrossRef]

46. Hui, K.S.; Hui, K.N.; Dinh, D.A.; Tsang, C.H.; Cho, Y.R.; Zhou, W.; Hong, X.; Chun, H.-H. Green synthesis of dimension-controlled silver nanoparticle–graphene oxide with in situ ultrasonication. *Acta Mater.* **2014**, *64*, 326–332. [CrossRef]

47. Biesinger, M.C. Accessing the robustness of adventitious carbon for charge referencing (correction) purposes in XPS analysis: Insights from a multi-user facility data review. *Appl. Surf. Sci.* **2022**, *597*, 153681. [CrossRef]

48. Al-Gaashani, R.; Najjar, A.; Zakaria, Y.; Mansour, S.; Atieh, M.A. XPS and structural studies of high quality graphene oxide and reduced graphene oxide prepared by different chemical oxidation methods. *Ceram. Int.* **2019**, *45*, 14439–14448. [CrossRef]

49. Ferraria, A.M.; Carapeto, A.P.; Botelho do Rego, A.M. X-ray photoelectron spectroscopy: Silver salts revisited. *Vacuum* **2012**, *86*, 1988–1991. [CrossRef]

50. Khairy, M.; Mohamed, M.M.; Ibrahem, A. Enhanced the Catalytic activity of reduction of 4-nitrophenol on Ag/RGO nanocomposites. *J. Bas. Environ. Sci.* **2018**, *5*, 101–114.

51. Bîru, E.I.; Iovu, H. Graphene Nanocomposites Studied by Raman Spectroscopy. In *Raman Spectroscopy*; Do Nascimento, G.M., Ed.; IntechOpen: London, UK, 2018; pp. 179–201. [CrossRef]

52. Allen, M.J.; Tung, V.C.; Kaner, R.B. Honeycomb Carbon: A Review of Graphene. *Chem. Rev.* **2010**, *110*, 132–145. [CrossRef]

53. Chen, J.; Yao, B.; Li, C.; Shi, G. An improved Hummers method for eco-friendly synthesis of graphene oxide. *Carbon* **2013**, *64*, 225–229. [CrossRef]

54. Wu, X.; Jaatinen, E.; Sarina, S.; Zhu, H.Y. Direct photocatalysis of supported metal nanostructures for organic synthesis. *J. Phys. D: Appl. Phys.* **2017**, *50*, 283001. [CrossRef]

55. Anandkumar, M.; Vinothkumar, G.; Babu, K.S. Synergistic effect of gold supported on redox active cerium oxide nanoparticles for the catalytic hydrogenation of 4-nitrophenol. *New J. Chem.* **2017**, *41*, 6720–6729. [CrossRef]

56. Strachan, J.; Barnett, C.; Masters, A.F.; Maschmeyer, T. 4-Nitrophenol Reduction: Probing the Putative Mechanism of the Model Reaction. *ACS Catal.* **2020**, *10*, 5516–5521. [CrossRef]

57. Karuppusamy, S.; Marken, F.; Kulandainathan, M.A. Role of Dissolved Oxygen in Nitroarene Reduction Catalyzed by a Heterogeneous Silver Textile Catalyst in Water. *New J. Chem.* **2020**, *44*, 17780–17790. [CrossRef]

58. Wunder, S.; Polzer, F.; Lu, Y.; Mei, Y.; Ballauff, M. Kinetic Analysis of Catalytic Reduction of 4-Nitrophenol by Metallic Nanoparticles Immobilized in Spherical Polyelectrolyte Brushes. *J. Phys. Chem. C* **2010**, *114*, 8814–8820. [CrossRef]

59. Jiang, S.; Wang, L.; Duan, Y.; An, J.; Luo, Q.; Zhang, Y.; Tang, Y.; Huang, J.; Zhang, B.; Liu, J.; et al. A novel strategy to construct supported silver nanocomposite as an ultrahigh efficient catalyst. *Appl. Catal. B: Environ.* **2021**, *283*, 119592. [CrossRef]

60. Shi, Y.; Zhang, X.; Zhu, Y.; Tan, H.; Chen, X.; Lu, Z.-H. Core-shell structured nanocomposites Ag@CeO₂ as catalyst for hydrogenation of 4-nitrophenol and 2-nitroaniline. *RSC Adv.* **2016**, *6*, 47966–47973. [CrossRef]

61. Chernykh, M.V.; Mikheeva, N.N.; Zaikovskii, V.I.; Mamontov, G.V. Influence of the Ag Content on the Activity of Ag/CeO₂ Catalysts in the Reduction of 4-Nitrophenol at Room Temperature and Atmospheric Pressure. *Kinet. Catal.* **2020**, *61*, 708–715. [CrossRef]

62. Kharlamova, T.S.; Salina, M.V.; Svetlichnyi, V.A.; Salaev, M.A.; Stadnichenko, A.I.; Mamontov, G.V. CeO₂-supported Pt–Ag bimetallic catalysts for 4-nitrophenol reduction. *Catal. Today* **2022**, *384–386*, 12–24. [CrossRef]

63. Kohantorabi, M.; Gholami, M.R. MₓNi₁₀₀₋ₓ (M = Ag, and Co) Nanoparticles Supported on CeO₂ Nanorods Derived from Ce-Metal Organic Frameworks as an Effective Catalyst for Reduction of Organic Pollutants: Langmuir-Hinshelwood Kinetics and Mechanism. *New J. Chem.* **2017**, *41*, 10948–10958. [CrossRef]

64. Lei, G.; Ma, J.; Li, Z.; Fan, X.; Peng, W.; Zhang, G.; Zhang, F.; Li, Y. Magnetic Au-Ag-γ-Fe₂O₃/rGO Nanocomposites as an Efficient Catalyst for the Reduction of 4-Nitrophenol. *Nanomaterials* **2018**, *8*, 877. [CrossRef]

65. Qu, J.; Ren, C.; Dong, Y.; Chang, Y.; Zhou, M.; Chen, X. Facile synthesis of multifunctional graphene oxide/AgNPs-Fe₃O₄ nanocomposite: A highly integrated catalysts. *Chem. Eng. J.* **2012**, *211–212*, 412–420. [CrossRef]

66. Joshi, M.K.; Pant, H.R.; Kim, H.J.; Kim, J.H.; Kim, C.S. One-pot synthesis of Ag-iron oxide/reduced graphene oxide nanocomposite via hydrothermal treatment. *Colloids Surf. A* **2014**, *446*, 102–108. [CrossRef]

67. Varshney, S.; Bar-Ziv, R.; Zidki, T. On the Remarkable Performance of Silver-based Alloy Nanoparticles in 4-nitrophenol Catalytic Reduction. *ChemCatChem* **2020**, *12*, 4680–4688. [CrossRef]

68. Li, W.; Ge, X.; Zhang, H.; Ding, Q.; Ding, H.; Zhang, Y.; Wang, G.; Zhang, H.; Zhao, H. Hollow Mesoporous SiO_2 Spheres Nanoarchitecture with Encapsulated Silver Nanoparticles for Catalytic Reduction of 4-nitrophenol. *Inorg. Chem. Front.* **2016**, *3*, 663–670. [CrossRef]

69. Shi, Y.; Zhang, X.-L.; Feng, G.; Chen, X.; Lu, Z.-H. Ag-SiO_2 nanocomposites with plum-pudding structure as catalyst for hydrogenation of 4-nitrophenol. *Ceram. Int.* **2015**, *41*, 14660–14667. [CrossRef]

70. Xiao, Z.-Y.; Huang, S.-X.; Zhai, S.-R.; Zhai, B.; Zhang, F.; An, Q.-D. PMHS-reduced fabrication of hollow Ag–SiO_2 composite spheres with developed porosity. *J. Sol-Gel Sci. Technol.* **2015**, *75*, 82–89. [CrossRef]

71. Bano, M.; Ahirwar, D.; Thomas, M.; Naiko, G.A.; Sheikh, M.U.D.; Khan, F. Hierarchical synthesis of silver monoliths and their efficient catalytic activity for the reduction of 4-Nitrophenol to 4-Aminophenol. *New J. Chem.* **2016**, *40*, 6787–6795. [CrossRef]

72. Soysal, F.; Çıplak, Z.; Gökalp, C.; Getiren, B.; Yildiz, N. One-step hydrothermal synthesis of nitrogen doped reduced graphene oxide-silver nanocomposites: Catalytic performance. *Appl. Organomet. Chem.* **2020**, *34*, e5621. [CrossRef]

73. Duan, C.; Liu, C.; Meng, X.; Lu, W.; Ni, Y. Fabrication of carboxymethylated cellulose fibers supporting Ag NPs@MOF-199s nanocatalysts for catalytic reduction of 4-nitrophenol. *Appl. Organomet. Chem.* **2019**, *33*, e4865. [CrossRef]

74. Chang, S.; Liu, C.; Sun, Y.; Yan, Z.; Zhang, X.; Hu, X.; Zhang, H. Fe_3O_4 Nanoparticles Coated with Ag-Nanoparticle-Embedded Metal−Organic Framework MIL-100(Fe) for the Catalytic Reduction of 4-Nitrophenol. *ACS Appl. Nano Mater.* **2020**, *3*, 2302–2309. [CrossRef]

75. Liu, G.-F.; Qiao, X.-X.; Cai, Y.-L.; Xu, J.-Y.; Yan, Y.; Karadeniz, B.; Lu, J.; Cao, R. Aluminum Metal−Organic Framework−Silver Nanoparticle Composites for Catalytic Reduction of Nitrophenols. *ACS Appl. Nano Mater.* **2020**, *3*, 11426–11433. [CrossRef]

76. Liu, B.H.; Li, Z.P. A review: Hydrogen generation from borohydride hydrolysis reaction. *J. Power Sources* **2009**, *187*, 527–534. [CrossRef]

77. Pinheiro, D.; Devi, K.R.S.; Jose, A.; Karthik, K.; Sugunan, S.; Mohan, M.K. Experimental Design for Optimization of 4-Nitrophenol Reduction by Green Synthesized CeO_2/g-C_3N_4/Ag Catalyst Using Response Surface Methodology. *J. Rare Earths* **2020**, *38*, 1171–1177. [CrossRef]

78. Hummers, W.S.; Offeman, R.E. Preparation of Graphitic Oxide. *J. Am. Chem. Soc.* **1958**, *80*, 1339. [CrossRef]